

See discussions, stats, and author profiles for this publication at: <https://www.researchgate.net/publication/262977578>

Structural Insights into the Coenzyme Mediated Monomer–Dimer Transition of the Pro–Apoptotic Apoptosis Inducing Factor

ARTICLE in **BIOCHEMISTRY** · JUNE 2014

Impact Factor: 3.02 · DOI: 10.1021/bi500343r · Source: PubMed

CITATIONS

2

READS

111

11 AUTHORS, INCLUDING:



[Marta Martínez-Júlez](#)

University of Zaragoza

75 PUBLICATIONS 1,034 CITATIONS

[SEE PROFILE](#)



[Patricio Fernández-Silva](#)

University of Zaragoza

53 PUBLICATIONS 2,946 CITATIONS

[SEE PROFILE](#)



[Anabel Gracia Lostao](#)

University of Zaragoza

48 PUBLICATIONS 463 CITATIONS

[SEE PROFILE](#)



[Milagros Medina](#)

University of Zaragoza

150 PUBLICATIONS 2,686 CITATIONS

[SEE PROFILE](#)

Structural Insights into the Coenzyme Mediated Monomer–Dimer Transition of the Pro-Apoptotic Apoptosis Inducing Factor

Patricia Ferreira,^{†,‡,§,¶} Raquel Villanueva,^{†,‡,§,¶} Marta Martínez-Júlvez,^{†,‡} Beatriz Herguedas,^{†,‡} Carlos Marcuello,[§] Patricio Fernandez-Silva,[†] Lauriane Cabon,^{||,‡,¶} Juan A. Hermoso,[●] Anabel Lostao,^{§,○} Santos A. Susin,^{||,‡,¶} and Milagros Medina^{*,†,‡}

[†]Departamento de Bioquímica y Biología Molecular y Celular, [‡]Instituto de Biocomputación y Física de Sistemas Complejos (BIFI)-Joint Unit BIFI-IQFR (CSIC), and [§]Laboratorio de Microscopias Avanzadas, Instituto de Nanociencia de Aragón (INA), Universidad de Zaragoza, Zaragoza, Spain

^{||}INSERM U1138, Cell Death and Drug Resistance in Lymphoproliferative Disorders Team, Centre de Recherche des Cordeliers, F-75006, Paris, France

[¶]Université Pierre et Marie Curie-Sorbonne Universités, F-75006, Paris, France

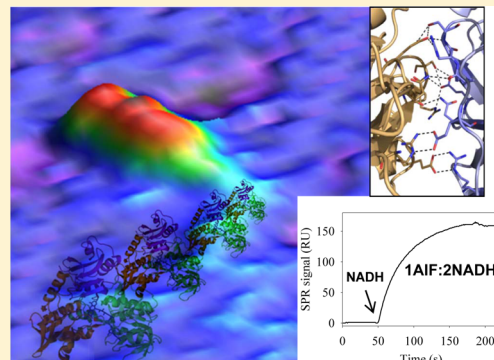
[#]Université Paris Descartes-Sorbonne Paris Cité, F-75006, Paris, France

[●]Instituto de Química Física Rocasolano, CSIC, Madrid, Spain

[○]Fundación ARAID, Zaragoza, Spain

Supporting Information

ABSTRACT: The apoptosis-inducing factor (AIF) is a mitochondrial flavoprotein that, after cell death induction, is distributed to the nucleus to mediate chromatinolysis. In mitochondria, AIF is present in a monomer–dimer equilibrium that after reduction by NADH gets displaced toward the dimer. The crystal structure of the human AIF (hAIF):NAD(H)-bound dimer revealed one FAD and, unexpectedly, two NAD(H) molecules per protomer. A 1:2 hAIF:NAD(H) binding stoichiometry was additionally confirmed in solution by using surface plasmon resonance. The here newly discovered NAD(H)-binding site includes residues mutated in human disorders, and accommodation of the coenzyme in it requires restructuring of a hAIF portion within the 509–560 apoptogenic segment. Disruption of interactions at the dimerization surface by production of the hAIF E413A/R422A/R430A mutant resulted in a nondimerizable variant considerably less efficiently stabilizing charge-transfer complexes upon coenzyme reduction than WT hAIF. These data reveal that the coenzyme-mediated monomer–dimer transition of hAIF modulates the conformation of its C-terminal proapoptotic domain, as well as its mechanism as reductase. These observations suggest that both the mitochondrial and apoptotic functions of hAIF are interconnected and coenzyme controlled: a key information in the understanding of the physiological role of AIF in the cellular life and death cycle.



The apoptosis-inducing factor (AIF) is a flavoprotein that mediates caspase-independent programmed cell death (PCD).^{1,2} Its gene is located on chromosome X, regions A6 and Xq25–26 in mice and humans, respectively.³ Human AIF (hAIF) is expressed as an apoprotein precursor (613 residues) that contains a N-terminal mitochondrial localization sequence (MLS) and two nuclear leading sequences (NLS).¹ After import in the mitochondria, the proteolytic cleavage of its N-terminal 54 residues produces the mature form of the protein, hAIF_{Δ1–54}. This form is inserted into the inner mitochondrial membrane, incorporating the FAD cofactor and folding in three structural domains.⁴ The FAD-binding and the NAD-binding domains show the classical Rossmann topology found in many other flavoproteins and confer to AIF a NAD(P)H dependent reductase activity,⁵ while the C-terminal is considered the pro-apoptotic region.^{6–8} After a cellular apoptotic insult, hAIF_{Δ1–54} is cleaved at residue 102 by calpains and/or cathepsins, yielding

a soluble and pro-apoptogenic form, hAIF_{Δ1–102}. hAIF_{Δ1–102} is translocated first to the cytoplasm and then to the nucleus, where it induces apoptosis by chromatin condensation and large scale DNA fragmentation.^{9–11} The identification of two alternative spliced mRNA isoforms of AIF, named AIFsh and AIFsh2, which correspond to the C-terminal and the reductase domains of AIF, respectively, initially suggested that the reductase and the apoptotic functions might be dissociated.^{7,12}

In addition to its apoptotic function, AIF appears to play a vital but unclear role in redox metabolism of healthy cells. Phenotypes associated with AIF deficiency and defects in both cellular and animal models suggest that its reductase activity

Received: March 20, 2014

Revised: June 10, 2014

Published: June 10, 2014

regulates mitochondrial structure and redox metabolism.^{13,14} AIF deficiency is also related to respiratory defects in mitochondrial complexes I and III, suggesting that its reductase activity might regulate oxidative phosphorylation by contributing to their assembly or by providing them with reducing power.¹⁵ More recently, mitochondrial human disorders featuring neurodegeneration have been associated with mutations in hAIF. Deletion of R201¹⁶ and G308E replacement¹⁷ are associated with the early onset of severe neuromuscular symptoms (including general delay and regression in psychomotor development, brain anomalies, hypotonia and hyporeflexia, seizures, muscle wasting and weakness) leading to considerably short lifespans. Patients affected by these two mutations also showed signs of mitochondrial abnormalities and impaired oxidative phosphorylation. Additionally, the E493V mutation is the genetic cause of the type 4, X-linked form of the Charcot-Marie-Tooth disease, Cowchock syndrome, a hereditary peripheral neuropathy associated with deafness and cognitive impairment.¹⁸ Evidence for the reductase activity of AIF supporting energy metabolism as well as benefiting the growth and invasiveness of advanced prostate cancer cells further indicates a relationship between the dual AIF action as a pro-life and as a pro-death effector.¹⁹ The study of the AIF molecular and oxido-reductase properties showed that its *in vitro* reduction by NADH occurs through the appearance of charge transfer complexes (CTC), inducing protein dimerization as well as conformational rearrangements of the reductase and the apoptogenic domains.^{4,5,18,20–22}

The identified pathogenic hAIF mutations and the interest in the design of new therapies to modulate caspase-independent apoptosis pathways make AIF a potential target to treat pathological disorders (cancer or degenerative diseases) in which this protein causes a defect or excess of apoptosis.²³ Since one of the possibilities for modulating the AIF pro-apoptotic function might be regulating its reductase activity,¹³ as well as its coenzyme dependent dimerization ability, it is of interest to further understand at the molecular level the parameters underlying such mechanisms in the human enzyme. Here, we present the crystal structure of the hAIF_{Δ1–102}:NAD(H) complex, revealing one FAD and, unexpectedly, two NAD(H) molecules per protomer. Proof of the critical *in vivo* functionality of the here newly discovered coenzyme-binding site of hAIF is given by the fact that two of the three detected human neuropathies above-mentioned are due to defects in its sequence, deletion of R201 and E493V mutation, correspond to this novel NAD(H) binding site.^{16,18} We have also characterized a mutant of hAIF_{Δ1–102} where, based on the structural data, the dimerization surface has been altered. The effects introduced by the mutations on protein dimerization, coenzyme binding, and kinetic parameters for the reductase activity indicate that the coenzyme-mediated monomer–dimer transition of hAIF modulates its mechanism as reductase.

■ EXPERIMENTAL PROCEDURES

Production of hAIF Proteins. The gene encoding the hAIF deletion mutant Δ1–102, hAIF_{Δ1–102}, was cloned into the pET28 expression vector with a cleavable N-terminal 6His-tag, and the pET28-hAIF_{Δ1–102} construct was used to transform *Escherichia coli* BL21(DE3) cells.¹² The plasmid encoding for the E413A/R422A/R430A hAIF_{Δ1–102} was obtained by site-directed mutagenesis on pET28-hAIF_{Δ1–102} at Mutagenex. Wild-type (WT) and E413A/R422A/R430A hAIF_{Δ1–102} were

expressed and purified as described in the Supporting Information (SI).

Molecular Weight Determination by Size Exclusion Chromatography. 90 μM WT and E413A/R422A/R430A hAIF_{Δ1–102}, either in the presence or absence of a 10-fold excess of NADH, were loaded onto a HiPrep 26/60 SephacrylS-200 high resolution (GE Healthcare) column attached to a fast pressure liquid chromatographic system (GE Healthcare), in 50 mM Tris-HCl, pH 8.0, 200 mM NaCl, at a flow rate of 0.5 mL/min. The column was calibrated with a LMW calibration kit (six proteins in the 6400–160000 Da range).

Stabilization of Cross-Linked Oligomers. Reaction mixtures containing 2–5 μM WT or E413A/R422A/R430A hAIF_{Δ1–102}, in 10 mM phosphate, pH 8.0 and a 100-fold excess of the homobifunctional-bis[sulfosuccinimidyl]-suberate (BS³, Pierce) cross-linker were incubated 30 min at 25 °C either in the absence or presence of 2 mM NADH. Reactions were terminated by addition of the denaturing bromophenol blue sample buffer. The mixture was resolved by 12% SDS-PAGE.

Atomic Force Microscopy Imaging. Atomic force microscopy (AFM) measurements were performed with a Cervantes Fullmode scanning probe microscope (Nanotec Electrónica S.L.). Images were taken using the Jumping Mode²⁴ with V-shaped silicon nitride cantilevers with integrated pyramidal 2 nm ultrasharp tips and spring constants of 0.01–0.03 N/m (Bruker Probes) in 0.5 μM solutions of hAIF_{Δ1–102} in PBS pH 7.0 at 20 °C, unless otherwise stated. The enzyme was also incubated with 50 μM NADH, NADPH, NAD⁺ or NADP⁺ at 4 °C for 10 min under mild stirring. When indicated, protein samples were pretreated with 100 μM of BS³ for 50 min at 25 °C in the presence of NADH, and the cross-linked mixtures were separated using 50 kDa filters (Amicon). hAIF_{Δ1–102} immobilization, image processing, and estimation of percentages for the different oligomeric states are described in SI.

Determination of the *in vivo* Association State of AIF by Native Polyacrylamide Electrophoresis. Mitochondria were isolated from mouse liver, mouse heart, HeLa cells, and mouse embryonic fibroblasts (MEFs) as described elsewhere.^{25–27} All procedures using mice were carried out under Project License 212-328 approved by the in-house Ethic Committee for Animal Experiments from the University of Zaragoza. The care and use of animals were performed accordingly with the Spanish Policy for Animal Protection RD53/2013, which meets the European Union Directive 2010/63 on the protection of animals used for experimental and other scientific purposes. Digitonin-solubilized mitochondrial proteins (10 μg per lane) were separated on clear native gradient gels (4–15% acrylamide) with cathode buffer containing 0.02% *n*-dodecyl β-D-maltoside by high-resolution clear native electrophoresis-1.²⁸ When appropriate, samples were incubated for 15 min with various NADH concentrations, before loading on the gels. AIF was detected by Western blot as indicated in SI.

Crystal Growth, Data Collection, and Structure Refinement. Crystals of the reduced hAIF_{Δ1–102}:NAD(H) complex were generated from a mixture containing oxidized hAIF_{Δ1–102ox} (150 μM) in 20 mM Tris-HCl, pH 8.0, 0.15 M NaCl, 10% glycerol with NADH (18 mM in H₂O). One microliter of this mixture was added to 1 μL of mother liquid containing 16–20% PEG 4K, 0.2 M Li₂SO₄, and 0.1 M Tris-HCl, pH 8.5. The resulting drops were equilibrated against 0.5 mL of mother liquid. Drops were set in an anaerobic glovebox

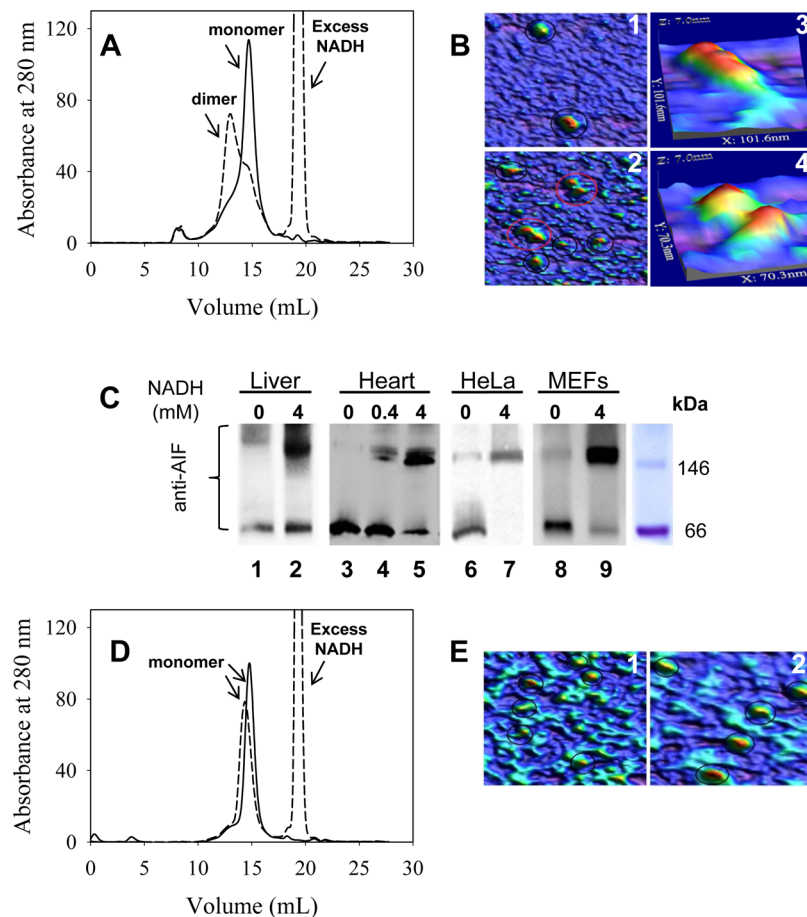


Figure 1. Aggregation states of recombinant and mitochondrial hAIF. (A) Elution profile on a Sephadex S-200 column of WT hAIF $_{\Delta 1-102}$ in 50 mM Tris-HCl pH 8.0, 200 mM NaCl. Continuous line corresponds to the free enzyme, while dashed line shows the profile upon incubation with a 10-fold excess of NADH. (B) Jumping mode-AFM topography 3-D images of (1) hAIF $_{\Delta 1-102ox}$; (2) hAIF $_{\Delta 1-102}$ incubated with NADH; and (3, 4) details of a monomer (the protein organization in three domains can be appreciated) and a dimer, respectively. Monomers and dimers are represented with black and red circles, respectively. Images obtained in PBS, pH 7.0. The area of the images in (1) and (2) corresponds to 300 nm 2 . The image in (2) was the originally scanned, while the rest are zoomed images of original AFM scans of a 500 nm 2 . (C) Western blot of digitonin-solubilized mitochondrial fractions obtained from mouse liver (lanes 1 and 2), mouse heart (lanes 3–5), HeLa cells (lanes 6 and 7), and MEFs cells (lanes 8 and 9) after separation by high-resolution clear native gel electrophoresis-1. The blot was probed with AIF specific antibodies. The concentration of NADH added to samples prior to electrophoresis is indicated. Molecular markers are indicated at the right side. (D) Elution profile on a Sephadex S-200 column of E413A/R422A/R430A hAIF $_{\Delta 1-102}$. Conditions and sample identification as in panel A. (E) Jumping mode-AFM topography 3-D images for E413A/R422A/R430A hAIF $_{\Delta 1-102}$. (1) E413A/R422A/R430A hAIF $_{\Delta 1-102ox}$ and (2) E413A/R422A/R430A hAIF $_{\Delta 1-102}$ incubated with NADH. Most of the features were monomers (black circles), while dimers were hardly found in the sample. The image in (1) is the original scanned image, while (2) is a zoomed image of the original AFM scan of a 500 nm 2 . Other conditions as in panel B.

(COY) to avoid turnover. Blue crystals grew after 24–48 h at 18 °C and were frozen under anaerobic conditions using mother liquid plus 20% glycerol as cryoprotectant. X-ray data sets were collected on the ID23.1 beamline at ESRF (Grenoble, France) and processed, scaled, and merged with autoPROC.²⁹ Crystals belonged to the P3₂1 space group with unit cells $a = b = 120.7 \text{ \AA}$, $c = 343.4 \text{ \AA}$. The structure was solved by molecular replacement using Molrep from the CCP4 package³⁰ and the hAIF $_{\Delta 1-121ox}$ structure (PDB ID: 1M6I²¹) as initial model. The structure previously reported for hAIF $_{\Delta 1-121ox}$ (1M6I) has been further refined here as indicated in SI using as initial input files its own pdb and mtz files. Statistics for data collection and refinement for both molecules are in Table SI-1. Atomic coordinates and structure factors are deposited in the PDB with PDB ID: 4BUR for the complex of hAIF $_{\Delta 1-102rd}$ with NAD(H) and PDB ID: 4BV6 for the refined hAIF $_{\Delta 1-121ox}$ structure.

Surface Plasmon Resonance Measurements. Two samples of His-tagged hAIF $_{\Delta 1-102ox}$ were covalently immobilized

on two independent NTA sensor chips³¹ up to responses of 7400 and 2284 resonance units (RU). Interaction of these immobilized proteins with 25 μM and 250 μM NADH, respectively, was assayed using a Biacore T200 (GE Healthcare) biosensor in the Biacore HBS-P buffer at 60 μL/min and 25 °C. Binding stoichiometry of NADH to His-tagged hAIF $_{\Delta 1-102ox}$ was estimated using the equation: $S = (\text{MW}^{\text{AIF}} \times \text{RU}_{\text{max}}^{\text{NADH}}) / (\text{MW}^{\text{NADH}} \times \text{RU}_{\text{max}}^{\text{AIF}})$, where RU_{max}^{NADH} refers to the theoretical maximal binding capacity extrapolated from the experimentally immobilized His-tagged hAIF $_{\Delta 1-102ox}$. RU_{max}^{AIF} is directly obtained by the sensogram recorded during ligand immobilization, and MW^{AIF} and MW^{NADH} are the corresponding molecular weights. The reference channel does not show significant nonspecific binding.

Spectroscopic Measurements. Spectroscopic and steady-state kinetic analyses were performed in a Cary 100 Bio spectrophotometer (Varian). Concentrations were determined using the molar absorbances of WT and E413A/R422A/R430A

hAIF_{Δ1–102} estimated by released free FAD with 3 M guanidinium chloride (ϵ_{450} 137767 and ϵ_{450} 12329 M⁻¹ cm⁻¹ respectively). Photoreduction of ~15 μM hAIF_{Δ1–102} was carried out at 18 °C using an anaerobic cuvette in 50 mM Tris-HCl, pH 8.0, with 2 mM EDTA and 5 μM 5-deazariboflavin.³² Reduction was also investigated with an excess of sodium dithionite, under both anaerobic and aerobic conditions. Steady-state activities of hAIF_{Δ1–102} were measured as described in SI.

Transient Kinetics Measurements. Stopped-flow measurements were carried out under both anaerobic and air-saturated conditions in an SX17.MV spectrometer (Appl. Phot. Ltd.) with a diode-array detector and the Xscan software. Tonometers containing enzyme or substrate solutions were made anaerobic by successive evacuation and flushing with argon.³³ Measurements were carried out in 50 mM phosphate, pH 8.0, at 25 °C with 8 μM hAIF_{Δ1–102} and a range of NAD(P)H concentrations (0.03–5 mM). Given concentrations are the final ones after mixing. Parameters were calculated as indicated in SI.

RESULTS

Dimerization of hAIF_{Δ1–102}. The recombinant WT hAIF_{Δ1–102} was obtained as a soluble and folded protein with the typical FAD maxima at 380 and 451 nm and a shoulder at 467 nm, indicating that the cofactor was in the oxidized state and correctly incorporated (Figure SI-1). Gel filtration chromatography indicated that hAIF_{Δ1–102ox} was a monomer with an apparent molecular weight of ~65 kDa, while hAIF_{Δ1–102} previously treated with NADH under aerobic conditions showed an additional peak with an apparent molecular weight of ~150–180 kDa (Figure 1A). The oligomer:monomer ratio was in the 2.3–2.7 range. Spectroscopic analysis of the oligomeric peak confirmed it corresponded to a hAIF_{Δ1–102rd}:NAD⁺ CTC (data not shown). Thus, NADH induced oligomerization of hAIF_{Δ1–102}. The nature of the hAIF_{Δ1–102ox} and hAIF_{Δ1–102rd}:NAD⁺ species was further characterized at the AFM single-molecule level to direct imaging single oligomers on mica surfaces, a method preserving catalytic activity (Figure 1B),³⁴ and to unequivocally identify their quaternary organization. AFM images of hAIF_{Δ1–102ox} revealed a homogeneous distribution of isolated molecules of diameter 7 ± 1 nm, that corresponded to the dimensions for the monomeric crystallographic structure (~5 × 6 × 7 nm) (Figure 1B, panels 1 and 3, and Table 1). Treatment of hAIF_{Δ1–102ox} with NAD(P)H increased the percentage of dimers over monomers (Figure 1B, panels 2 and 4), confirming that dimers were the quaternary organization representing the hAIF_{Δ1–102rd}:NAD⁺ CTC. Production of dimers was particularly evident upon treatment with NADH over NADPH, suggesting lower enzyme affinity for NADPH. The oxidized form of the coenzyme, NAD⁺, did not produce dimerization. Most of the dimers showed asymmetrical compositions and, although neatly distinguishable, it was not possible to assign intermolecular interactions between domains. Increasing the concentration of hAIF_{Δ1–102ox} significantly increased the percentages of oligomers (Table 1), including trimers and other higher aggregates.

The association state of AIF in mitochondria from mouse liver, heart, and MEFs cells, as well as from human HeLa cells was investigated by using blue native electrophoresis (Figure 1C). In whole digitonin-solubilized mitochondrial fractions, native AIF was mainly present as a monomer, while treatment

Table 1. Distribution of Monomers and Dimers Identified by AFM for WT and E413A/R422A/R430A hAIF_{Δ1–102} under Different Conditions^a

preincubation conditions	monomers (%)	dimers (%)
WT	96	4
WT	NQ	NQ
WT 5x	96	4
WT + NAD ⁺	48	52
WT + NADH	87	13
WT + NADP ⁺	66	33
WT + NADPH	96	4
E413A/R422A/R430A	90	10
E413A/R422A/R430A + NADH	96	4
E413A/R422A/R430A + NADH + BS ³	90	10

^aProtein concentration for the incubation on the mica was 0.5 μM in PBS pH 7.0. Percentages refer to the total protein molecules, independently on the association state. Error associated with the percentages is within 5–15%. NQ: nonquantifiable and corresponding to a fraction of molecules including trimers and higher aggregates.

with exogenous NADH greatly increased dimerization. This observation slightly differs from previously reported data in the rodent liver fraction of mitochondria,²⁰ where mAIF was reported to exist as an equimolar mixture of monomers and dimers. Altogether, these results encouraged us to further analyze the molecular determinants controlling the dimerization of human AIF.

The hAIF_{Δ1–102rd}:NAD(H) Interaction at the Molecular and Atomic Levels. The hAIF_{Δ1–102rd}:NAD(H) structure was solved at 2.9 Å resolution with final R and R_{free} factors of 0.18 and 0.23, respectively (Table SI-1). The four chains of the asymmetric unit present a similar overall fold: r.m.s.d. of 0.28 Å (412 C_ω chain B), 0.24 Å (373 C_ω C), and 0.30 Å (384 C_ω D) regarding chain A. The final atomic model contains residues 128–516 and 551–611 in chain A, 125–516 and 553–610 in B, 127–517 and 558–612 in C, and 128–509 and 559–611 in D, and electron density was clear to position one FAD and two NAD(H) molecules per hAIF_{Δ1–102} protomer with 100% occupancy (Figure 2). The blue color of the crystals indicated

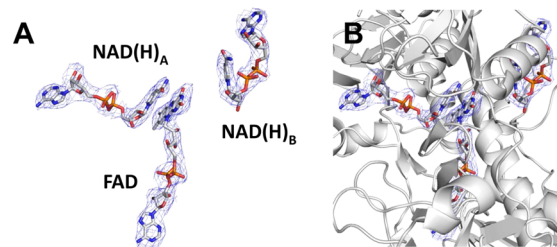


Figure 2. Electron density maps for hAIF ligands. (A) The $|F_o| - |F_c|$ electron density map shown at 2.0σ with the ligands modeled inside it. (B) Detail of the ligands electron density within the protein environment. NAD(H)_A, NAD(H)_B, and FAD are displayed in CPK sticks with carbons in white, while the protein backbone is shown in gray cartoon.

the flavin was reduced and forming a CTC with at least one NAD⁺ molecule. The nicotinamide rings of both coenzyme molecules show perfect planar organizations, which suggest both might be in the oxidized state. Therefore, herein we will refer to this complex as hAIF_{Δ1–102rd}:2NAD(H). The single FAD and the two NAD(H) molecules occupy identical positions in all chains (Figures 3 and 4). Analysis of association

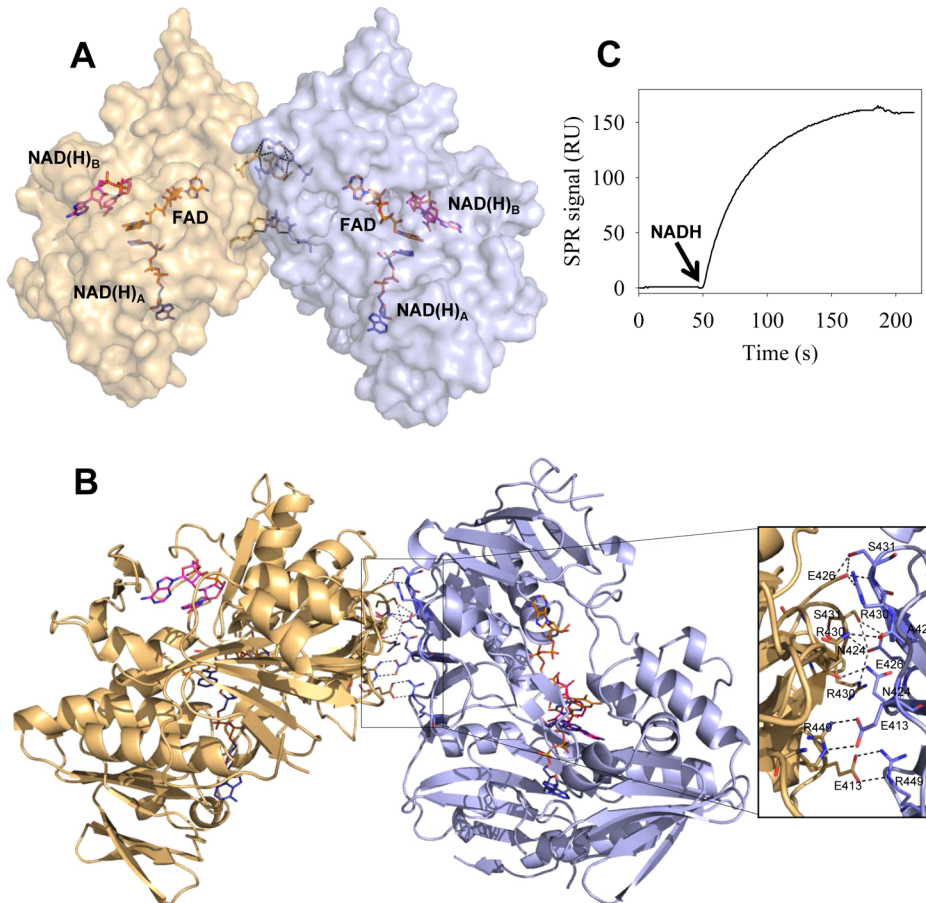


Figure 3. Structure of the hAIF_{Δ1–102rd}:2NAD(H) dimer. (A) Surface representation. Chains A and C are in pale yellow and blue, respectively. FAD, NAD(H)_A, and NAD(H)_B are shown as sticks with its C atoms in orange, blue, and pink, respectively. Residues at the interface are also represented as sticks (yellow and blue). (B) Cartoon representation. The interface residues are shown as sticks. A zoom of the interface area with interactions in dashed lines is also shown. (C) SPR sensogram showing the association of NADH (25 μM) with covalently immobilized His-tagged hAIF_{Δ1–102ox} on a NTA chip (7400 RUs) and the net resonance signal (RU) obtained by subtracting the reference channel from the experimental one. Measurements were carried out in Biacore HBS-P buffer at 60 μL/min and 25 °C. The injection of NADH (arrow) resulted in a 159 RU rise, indicating NADH binding with a ~1:1.8 stoichiometry.

of the four chains of the asymmetric unit of the hAIF_{Δ1–102rd}:2NAD(H) complex suggests as the most probable biological assembly in solution a dimer stabilized by several H-bonds and salt bridges, and represented by either the association of chains A and C, or of chains B and D (Figure 3B). The carboxylate of E426 from one protomer interacts with the O-gamma and N atoms of S431 from the other protomer, while N424 and A429 from each protomer are H-bounded to each other. The dimer is additionally stabilized by salt bridges between the carboxylic O-epsilon1 and O-epsilon2 atoms of E413 and the N-epsilon and NH2 of R449, and between N-epsilon of R430 and O-epsilon2 of E426 from each protomer. Finally, Arg422 residues from each protomer stack on each other through their guanidinium groups. These residues are conserved in mouse AIF (mAIF) and also involved in stabilization of its dimer.²² Superposition onto chain A of hAIF_{Δ1–102rd}:2NAD(H) of the refined hAIF_{Δ1–121ox} monomeric model (see SI) shows a r.m.s.d. of 1.108 Å (414 C_α atoms). These data suggest that binding of NADH to hAIF_{ox} plus the subsequent hydride transfer (HT) trigger dimerization of the protein. To confirm whether the enzyme:coenzyme stoichiometry found in the crystal was relevant in solution, complex formation between covalently immobilized hAIF_{Δ1–121ox} and

NADH was further analyzed using SPR. Sensograms obtained under conditions trying to mimic the crystallographic ones, 2280 RUs of immobilized His-tagged hAIF_{Δ1–102ox} and a high concentration of the NADH ligand (250 μM), yielded a 55 RU rise that indicated a 1:2 stoichiometry (not shown). When the amount of immobilized protein was increased by 3 times and that of NADH reduced by 10-fold, to mimic more physiological conditions, the determined stoichiometry was 1:1.8 (Figure 3C). These results agree with the hAIF_{Δ1–102rd}:2NAD(H) structure and confirm the presence of two NAD(H) binding sites in the enzyme.

Regarding these two NAD(H) molecules found in each protomer (Figures 3A and 4), the first one (herein NAD(H)_A) shows an extended conformation with its nicotinamide stacking in parallel between the *re*-face of the FAD flavin and the F310 rings (Figure 4B). Its binding is stabilized through a H-bond network involving G308, F310, L311, E314, E336, G399, E453, H454, and W483. Comparison with the free enzyme indicated displacements of F310 (3.6 Å) and H454 (2.9 Å) (Figure 4B) to accommodate the nicotinamide of NAD(H)_A, producing a stacking between the nicotinamide and flavin rings apparently optimal for charge transfer. Similarly to the free structure, P173, at the N-terminal of the 173–180 α helix, stacks against the

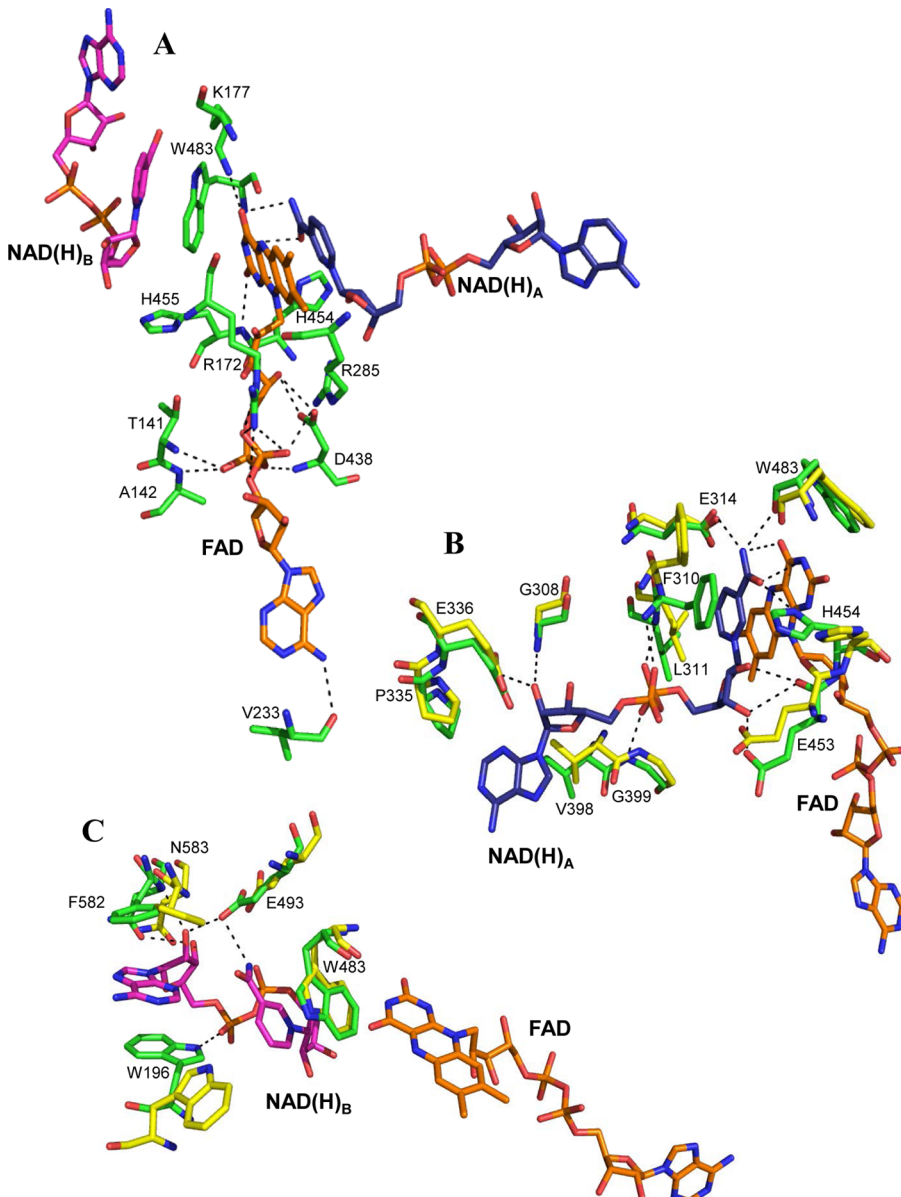


Figure 4. FAD and NAD(H) binding sites in the hAIF_{Δ1–102rd}:2NAD(H) complex. Network of H-bonds and hydrophobic stacking interactions at the (A) FAD binding site, (B) NAD(H)_A binding site, and (C) NAD(H)_B binding site. Carbon atoms are shown in orange for FAD, and blue and pink for NAD(H)_A and NAD(H)_B, respectively. Residues from hAIF_{Δ1–102ox} (panels B and C) are shown as yellow sticks and those of hAIF_{Δ1–102rd}:2NAD(H) as green.

pyrazine ring at the *si*-face of the flavin, while W483 closes its pyrimidine end with an angle of ~45°. The second NAD(H) molecule (NAD(H)_B), identified here for the first time, binds at the *si*-side of the flavin (Figure 4A,C), with its nicotinamide stacking at the other side of W483. NAD(H)_B binding induces displacement of F582 (2 Å) and, particularly, W196 (7 Å, plus rotation) to accommodate the adenine of NAD(H)_B through stacking interactions. W196 and E493 also contribute to stabilize the pyrophosphate, ribose, and nicotinamide moieties of the coenzyme.

In hAIF_{ox} the apoptotic C-terminal domain (residues 478–610) includes a long and flexible region (509–559) that apparently occludes access to the redox active site.⁴ Our refined hAIF_{Δ1–121ox} model provides additional information on this elusive, but key, fragment. A portion of this region folds into two short α -helices (517–524 and 529–533) (Figure 5A),

which decrease the accessibility of solvent to the flavin ring through W483. Residues following these two α -helices are organized in a loop (533–545) and, high flexibility beyond position 546 makes the rest of the region not visible (546–558). In the structure of the hAIF_{Δ1–102rd}:2NAD(H) complex residues previously forming the two short α -helices (517–524 and 529–533) are not observed anymore (Figure 5B), and their former position in the coenzyme free structure now allocates NAD(H)_B. Moreover, the loop 510–516 (connecting the end of a β -sheet with the helix 517–524 in hAIF_{ox}) is considerably displaced and transformed into the sixth antiparallel β strand of the β -sheet that now ends at N516 (compare Figure 5A,B). In hAIF_{ox} the 517–533 region is stabilized by direct interaction with the 190–202 β -hairpin, particularly by a H-bond and a salt-bridge between the side-chain of R201 and those of T526 and E531, respectively. Upon

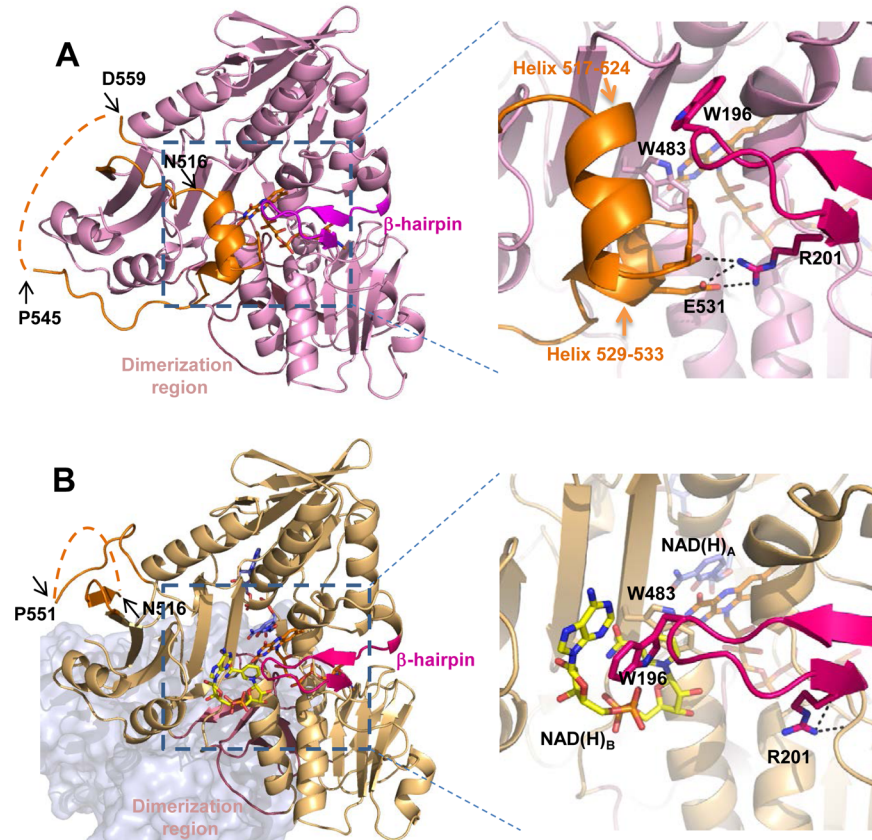


Figure 5. Conformational changes observed in hAIF upon NADH induced dimerization. Cartoon representation of (A) refined hAIF_{Δ1-121ox} (pink) and (B) hAIF_{Δ1-102rd}:2NAD(H) (wheat). Visible residues in the 508–560 segments are drawn in orange, residues involved in the dimerization surface in dark salmon and those of the β -hairpin in hot pink. FAD, NAD(H)_A, and NAD(H)_B are drawn in sticks with C in orange, blue, and yellow, respectively. Missing fragments are indicated as dotted orange lines. Enlarged regions show a detail of the NAD(H)_B binding site for each structure. In (B) the second protomer of the dimer is also shown as a gray surface.

coenzyme binding and/or reduction R201 results displaced by forming a H-bond with the main chains of Y204 and S202, thus, contributing to the unfolding of the short helices, allowing NAD(H)_B stabilization and releasing the orientation of the 190–202 β -hairpin to the solvent. Overall, these results uncover that at a molecular level the oxido-reduction and/or coenzyme bound status of hAIF modulates the conformation of its C-terminal proapoptotic domain. This is a key result in the comprehension of the double biological role of AIF.

The Dimerization Surface Modulates the Properties of hAIF_{Δ1-102}. To better understand the particular roles of the dimerization surface, we produced the E413A/R422A/R430A hAIF_{Δ1-102} variant. The purified mutant showed spectroscopic properties similar to the WT (Figure SI-1B), indicating similar folding around the oxidized flavin. Gel filtration analysis of E413A/R422A/R430A hAIF_{Δ1-102}, either in the absence of NADH or upon incubation with the coenzyme under aerobic conditions, indicated the protein was maintained as a monomer with apparent molecular weights of ~61 and ~77 kDa, respectively (Figure 1D). Given the apparently short life of the E413A/R422A/R430A hAIF_{Δ1-102rd}:NAD(H) complex, the BS³ cross-linker (conjugating mAIF dimers²²) was used to block the presumptive formation of the dimer upon incubation with NADH. After incubation of both E413A/R422A/R430A and WT hAIF_{Δ1-102ox} with a 100-fold excess of BS³, only a protein monomer of ~55 kDa was assessed by SDS-PAGE for both samples (Figure SI-2, lanes 3 and 6). However, when WT hAIF_{Δ1-102} was incubated with both BS³ and NAD(P)H, it

appeared mainly as a broad band covering the range of 130–170 kDa (Figure SI-2, lane 4). This MW range includes the value expected for the dimer, in agreement with the results obtained by gel filtration and AFM. However, only traces of dimers, if any, were detected for E413A/R422A/R430A hAIF_{Δ1-102} when treated under the same conditions (Figure SI-2, lane 7). AFM images of samples similarly treated confirmed E413A/R422A/R430A hAIF_{Δ1-102} as a monomeric species, even in the presence of the cross-linker and NADH (Figure 1E, Table 1). All together these data corroborate that the introduced mutations at the dimerization surface drastically affect the hAIF_{Δ1-102} capacity to dimerize, confirming the role of E413, R422, and R430 in the dimer stabilization.

At this point, it was necessary to identify whether the introduced mutations might have any effect in the protein properties as reductase. Even though the putative role of AIF as mitochondrial oxidoreductase remains elusive,¹³ one common experiment to unravel this potential role is to assay typical electron acceptors, as well as types of redox centers, as theoretical electron acceptors of NAD(P)H reduced hAIF.¹⁸ Determination of different activities confirmed that WT hAIF_{Δ1-102} does not exhibit NAD(P)H oxidase activity, that its redox partners are neither proteins containing iron–sulfur centers nor glutathione, and that it does not have any relevance in the *in vivo* bioreductive activation of quinones. DCPIP, ferricyanide, and Cytc were more efficient in accepting electrons from NADH reduced hAIF_{Δ1-102} (Table 2). When using those acceptors k_{cat} values were low and K_m^{NADH} large, and

Table 2. Kinetic Parameters for the Reduction of WT and E413A/R422A/R430A hAIF_{Δ1-102} by NADH^a

Steady-State Kinetic Parameters for the NADH Reductase Activity with Different Electron Acceptors			
electron acceptor	k_{cat} (s ⁻¹)	K_m^{NADH} (μM)	$k_{\text{cat}}/K_m^{\text{NADH}}$ (s ⁻¹ mM ⁻¹)
WT			
DCPIP ^b	1.5 ± 0.1	273 ± 31	5.6 ± 0.2
ferricyanide	3.1 ± 0.4	1375 ± 249	2.3 ± 0.4
Cyt c	0.6 ± 0.2	203 ± 75	6.4 ± 0.7
E413A/R422A/R430A			
DCPIP	0.5 ± 0.03	17 ± 7	28 ± 0.5
ferricyanide	1.6 ± 0.4	335 ± 147	4.8 ± 0.7
Cyt c	0.1 ± 0.01	39 ± 14	2.1 ± 0.5
Transient Kinetic Parameters for the Reductive-Half Reaction			
AIF _{Δ1-102} variant	k_{HT} (s ⁻¹)	K_d^{NADH} (μM)	$k_{\text{HT}}/K_d^{\text{NADH}}$ (s ⁻¹ M ⁻¹)
WT ^c	1.0 ± 0.1	1055 ± 302	976 ± 0.4
E413A/R422A/R430A	0.5 ± 0.01	2260 ± 295	221 ± 0.2

^aSteady-state assays were performed in 50 mM Tris-HCl, pH 8.0, at 25 °C, and pre-steady-state ones in 50 mM phosphate buffer, pH 8.0, at 25 °C. ^bThe WT diaphorase activity with DCPIP was also determined in 50 mM phosphate, pH 8.0, with similar kinetic constants than those here reported. Regarding specificity for the coenzyme, NADPH ($K_m^{\text{NADPH}} = 896 \mu\text{M}$ and $k_{\text{cat}} = 0.04 \text{ s}^{-1}$ for DCPIP) provided a catalytic efficiency 92-fold lower than NADH, pointing to NADH as the preferred reductant for hAIF_{Δ1-102}. ^cIncreasing ionic strength up to 140 mM produced a considerable decrease in the WT hAIF_{Δ1-102}:NADH affinity ($K_d^{\text{NADH}} = 5096 \mu\text{M}$, $k_{\text{HT}} = 2 \text{ s}^{-1}$). Additionally, k_{HT} and K_d for the WT form showed a clearly preference for NADH versus NADPH as electron donor (k_{cat} and K_d^{NADPH} were 12.5-fold lower and 4.5-fold higher than the corresponding with NADH), in agreement with steady-state kinetics.

in the same range than those reported for other AIF human and mouse isoforms (despite slight differences in experimental conditions; Table 1 from ref 18 and data from ref 13). The similar low efficiencies with Cyt c and the artificial electron acceptors reduce the possibilities of Cyt c being the *in vivo* hAIF_{Δ1-102} redox partner, even though both proteins are in the mitochondrial intermembrane space. E413A/R422A/R430A hAIF_{Δ1-102ox} was only slightly more efficient with either DCPIP or ferricyanide (5- and 2.2-fold, respectively) and slightly less in the Cyt c reductase assay (0.4-fold) (Table 2). Differences regarding the WT are just a consequence of slight differential decreases in both k_{cat} and K_m^{NADH} , suggesting that changes at the dimerization surface only have minor effects in these activities. Similarly to the WT, this variant did not present NADH oxidase activity.

The effects of mutations on coenzyme binding affinity and on the rate constant describing the HT step, k_{HT} , from NADH to the isoolloxazine of hAIF_{Δ1-102ox} were analyzed by stopped-flow transient kinetics. Similarly to that observed for the WT, HT from NADH to E413A/R422A/R430A hAIF_{Δ1-102ox} resulted in full reduction of the flavin with the concomitant formation of a broad band (~635 nm) consistent with the formation of a FADH⁻:NAD⁺ CTC (Figure 6). However, the CTC band considerably decreased in intensity (only ~30% of the WT process). This suggests either reduction of the percentage of CTC stabilized or the production of a CTC with different spectroscopic extinction coefficients (different charge distribution between the reacting rings). The transient observed rate constants, k_{obs} , for the WT process were

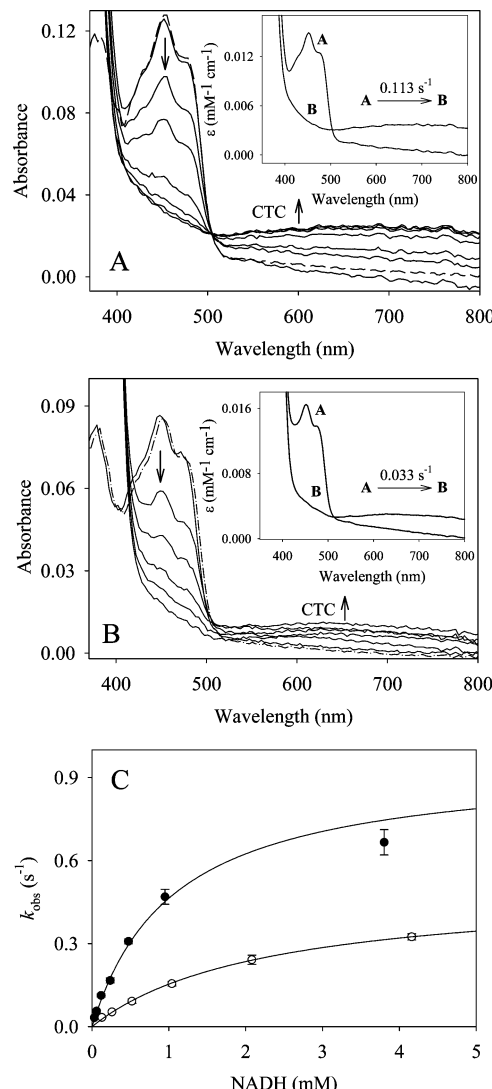


Figure 6. Spectral changes during the reduction of hAIF_{Δ1-102ox} by NADH. Spectra recorded for the reaction of NADH (150 μM) with (A) WT hAIF_{Δ1-102ox} (8 μM) at 0.03, 3.6, 6.9, 16.7, 26.5, 36.4, and 46 s after mixing; (B) E413A/R422A/R430A hAIF_{Δ1-102ox} (7 μM) at 0.03, 2.5, 5, 8, 11, and 16 s after mixing. The insets show the absorbance spectra for the intermediate species obtained by fitting the spectral evolution to a single step model (A → B). Dashed lines correspond to oxidized protein spectra before mixing. (C) Dependence of the observed reduction rates for the reduction of (●) WT and (○) E413A/R422A/R430A hAIF_{Δ1-102ox} on the concentration of NADH. All reactions were analyzed using a stopped-flow spectrophotometer in 50 mM phosphate buffer, pH 8.0 at 25 °C.

independent of the presence of molecular oxygen, CTC being stable for at least 3 days. Thus, and similarly to other AIF forms,^{5,20} hAIF_{Δ1-102rd} exhibits high affinity for the NAD(H) ligand that when bound prevents reoxidation by molecular oxygen. However, reaction for E413A/R422A/R430A hAIF_{Δ1-102ox} under aerobic conditions indicated quick reoxidation of the reduced species at low coenzyme concentrations and lack of CTC stabilization, while at higher concentrations the produced CTC had very short lifetimes. Herein k_{obs} values were calculated under anaerobic conditions, showing a hyperbolic dependence on the coenzyme concentration for all the variants (Figure 6C). This dependence allowed determining the k_{HT} , and the dissociation constant,

K_d^{NADH} , for the productive complexes (Table 2), with an essentially irreversible reduction envisaged from data fits. Kinetic parameters for E413A/R422A/R430A hAIF $_{\Delta 1-102\text{ox}}$ indicated that this variant resulted around 5-fold less efficient in oxidizing the coenzyme (k_{HT}/K_d of $221 \text{ s}^{-1} \text{ M}^{-1}$ versus $976 \text{ s}^{-1} \text{ M}^{-1}$) than the WT. Nevertheless, its k_{HT} was in the same range as k_{cat} for the DCPPIP diaphorase and Cyt c reductase activities, as for the WT enzyme, indicating that the HT step is the rate-limiting one.

■ DISCUSSION

Under physiological conditions in mitochondria, the monomeric state of native mAIF and hAIF appears to predominate over the dimeric form, while the proportion of dimers considerably increases upon binding of NADH and subsequent reduction of the flavin (Figure 1). This observation pointed us to gain further insights into the molecular determinants controlling protein dimerization obtaining the crystal structure of the dimer by incubation of hAIF $_{\Delta 1-102\text{ox}}$ with NADH. This structure shows the novelty of having two molecules of NAD(H) bound per protein protomer, hAIF $_{\Delta 1-102\text{rd}:2\text{NAD(H)}}$. This stoichiometry was also confirmed in solution by using SPR (Figure 3C). One of them, NAD(H) $_A$, was already described in the structure of the mAIF $_{\text{rd}}:\text{NAD}^+$ complex,^{4,22} but the second, NAD(H) $_B$, was not detected at that time. The redox active nicotinamide of NAD(H) $_B$ shows a parallel stacking against the side-chain of W483 that on the other face stacks against the pyrimidine ring of FAD. W483 is not displaced regarding the free structure, and its position prevents direct stacking between the nicotinamide and the isoalloxazine rings, forcing NAD(H) $_B$ into a bent conformation (Figures 4A and 4C). Comparison of hAIF $_{\Delta 1-102\text{rd}:2\text{NAD(H)}}$ with hAIF $_{\Delta 1-121\text{ox}}$ indicates that accommodation of NAD(H) $_B$ is assisted by ligand-binding and/or redox induced conformational changes in the 190–202 β -hairpin and in the 509–560 segment (Figure 5). Both regions are specific for mammalian AIF, being absent in its closest structural homologues.⁶ Although NAD(H) $_B$ was not detected in the mAIF $_{\text{rd}}:\text{NAD}^+$ structure, it showed the above-mentioned conformational changes as well as the preformed cavity for its binding.²² Moreover, docking analysis also predict binding of NAD(H) $_B$ in similar conformation than in the human structure (Figure SI-3). NAD(H) $_B$ is situated at the position of the two short helices of hAIF $_{\Delta 1-121\text{ox}}$ probably contributing to their disorder and preventing their stabilization through the 190–202 β -hairpin, particularly with R201 side-chain (Figure 5). Remarkably, a human mitochondrial encephalopathy is directly associated with the deletion of R201.^{16,18} Deletion of R201 might disrupt the interactions and organization established by the β -hairpin, and, therefore, of the rest of elements in contact with it, in both AIF $_{\text{ox}}$ and AIF $_{\text{rd}}:\text{NAD(H)}$. This will also include the conformational changes required during enzyme function and the stabilization of NAD(H) $_B$. *In vitro* this deletion mutant is an unstable protein with altered properties as reductase and increased affinity for DNA (a prerequisite for AIF-mediated nuclear apoptosis).¹⁶ This has been associated with the abnormally high percentage of DNA damage described in cells of patients carrying the R201 deletion.³⁵ On the contrary, replacement in mAIF of another residue of the β -hairpin, W195 (equivalent to W196 on hAIF), improved the enzyme efficiency as reductase.²² This was interpreted as this Trp being in the pathway of electrons coming to the surface from the flavins. However, the presence of NAD(H) $_B$ in the hAIF $_{\Delta 1-102\text{rd}}:\text{NAD(H)}$

(H) structure might suggest an alternative path, by involving its nicotinamide ring and W483 in the electron transfer pathway toward the surface (Figure SI-4). The Cowchock syndrome has also been associated with a mutation at the NAD(H) $_B$ site. It involves substitution of E493 by Val.¹⁸ Such mutation would prevent the interaction of the E493 side-chain with the two short helices in hAIF $_{\Delta 1-102\text{ox}}$ and with the ribose of NAD(H) $_B$ in hAIF $_{\Delta 1-102\text{rd}:2\text{NAD(H)}}$, explaining some of the effects reported for the E493V hAIF variant.^{18,20} Curiously, the AIFsh isoform, lacking the FAD and NAD(H) $_A$ binding regions (and therefore the reductase activity), but keeping the dimerization, NLS2 and main NAD(H) $_B$ binding regions, provokes the same apoptotic effects as hAIF $_{\Delta 1-102}$.⁷ Altogether, these data support the importance of the folding conservation in the region of AIF where NAD(H) $_B$ binds, indicating that the integrity of this site is required for the efficient action of the enzyme in living cells and probably also modulating the apoptotic activity.

When comparing the dimeric hAIF $_{\text{rd}}:\text{2NAD(H)}$ and mAIF $_{\text{rd}}:\text{NAD}^+$ structures with their corresponding free oxidized forms, it is clearly envisaged that NADH binding and the subsequent HT event induce the displacement of several residues and protein motifs (Figure S).²² Differences at the dimeric interface, formed by an intricate network of H-bonds and salt-bridges with a typical overrepresentation of arginine residues (Figure 3B),³⁶ are mainly concentrated in slight differences in the orientation of the backbone side-chains, as well as of R239 and the NLS2 at the borders, facts contributing to a good complementarity at the dimerization surface (Figures 3A, 3B and SI-5). The NLS2 region was proposed as the one inducing dimerization upon receiving the redox signal from the active site through the conformational shift of H454 (similarly observed in hAIF and mAIF, Figure 3B, and Figure 1D from ref 22 respectively). However, other factors might not be excluded. Thus, the large changes predicted in allocation and conformation of the 509–559 fragment upon coenzyme binding and flavin reduction, as well as the fact that the flavin is reduced, might have important effects in the electrostatic surface potential in protein regions different from the dimerization surface and, therefore, in the magnitude and orientation of the molecular dipole moment (Figure SI-6).

Here, we have particularly addressed the role of the dimer interaction surface by introducing mutations at the dimer interface that completely abolish detection of dimers (Figure 1D,E, Table 1). When compared to the WT, the non-dimerizable R413A/R422A/R430A mutant shows deleterious effects regarding the stabilization of CTCs, which also became reactive versus reoxidation by molecular oxygen. However, this mutant shows a slight increase in the catalytic efficiency, mainly as consequence of the decrease in K_m^{NADH} , while pre-steady-state analysis indicated that the HT process with the mutant was just slightly less efficient. All together this suggests that disruption of the dimerization surface has negative effects in the protein capacity to stabilize both the CTC and the dimer, indicating a relationship between the formation of these two species, and, therefore, a cross-talk between the NAD(H) binding sites and the dimerization surface. Furthermore, the low catalytic efficiencies and the high stability of the WT hAIF $_{\text{rd}}:\text{NAD}^+$ CTC dimer suggest that dissociation of NAD $^+$ limits the overall rate in the reaction, these appearing to be key characteristics of the WT enzyme to regulate its reductase activity. *In vivo*, and under the adequate cellular environment, such kinetic limitation might be overcome by interaction with the adequate physiological electron acceptor, which might decrease the

affinity for NAD⁺ within the hAIF_{rd}:NAD⁺ CTC dimer. The importance of the regulation on this process is also stated by the lethal effects in humans produced by mutations that improve the hAIF reductase efficiency and/or the reactivity of its reduced form versus different electron acceptors.^{16,18}

Lack of the mutant to stabilize different conformations, as the dimer, might influence also the interaction of AIF with its partners. No information is available about the surface of AIF interacting with other mitochondrial proteins, but some is known at the cytosolic and, particularly, nuclear levels.^{37–42} Upon AIF dimerization, secondary structural elements and their organization do not seem mainly altered neither at the CypA nor at the Hsp70 binding regions (Figure SI-5), but the accessibility to the surface of some of the atoms at those regions is altered and might modulate the expected interactions. Noteworthy, the CypA–AIF interaction appears to be stronger upon AIF reduction by the coenzyme.³⁹ Nevertheless, the coenzyme induced dimerization will clearly have a much more drastic effect on the interaction of those partners expected to recognize the S09–S59 fragment. This C-terminal insertion contains a proline/glutamic acid/serine/threonine-rich sequence (residues 529–560) usually involved in protein–protein interactions, modulation of the calpain proteolytic activity, or acting as proteolytic signal to mediate protein turnover via proteosomal degradation.⁴³ Additionally, it contains a Pro-rich motif (S44–S54, region not visible in the hAIF_{ox} crystal structure), a potential recognition and interaction site for proteins implicated in the regulation of different cellular processes and described as the interaction site of H2AX³⁸.

In conclusion, within the last years, hypotheses have come up with the two functions of AIF as a key factor for mitochondrial energy production and as a pro-death effector somehow related. Our data on different cellular types indicate that native AIF monomers are the predominant form in healthy mitochondria, undergoing dimerization upon NADH reduction. The NADH-bound dimer is stabilized by long-lived CTCs that *in vitro* protect from reoxidation by molecular oxygen. The crystal structure of reduced hAIF shows for the first time two bound NAD(H) molecules per protomer and indicates that the redox reorganization of the two specific insertions for mammalian AIF (the 190–202 β -hairpin and the 509–560 segment in the apoptotic domain) allows the accommodation of the second coenzyme molecule. The fact that several mitochondrial human disorders caused by AIF mutations are related to this second NAD(H)-binding active site, which remains in the apoptogenic AIFsh isoform, points to its importance for the efficient action of native hAIF in living and apoptotic cells. Therefore, AIF activities might be positively or negatively regulated by binding of the reduced form of the coenzyme in response of its availability in the environment. This observation is supported by the fact that mitochondria are the major stores of NAD(H), its redox status being an important modulator of mitochondrial function.^{44,45} This study further supports the fact that vital and lethal functions of AIF are coenzyme controlled.

ASSOCIATED CONTENT

Supporting Information

Methodology about production and purification of hAIF variants, atomic force microscopy imaging, steady-state and transient kinetics analysis, HeLa and MEFs cell cultures, Western blotting and refinement of the hAIF_{Δ1–121ox} structure (in Supporting Information of experimental procedures); Evolution of the WT spectrum along photoreduction, and

spectra for oxidized WT and E413A/R422A/R430A hAIF_{Δ1–102} (Figure SI-1), SDS patterns of WT and E413A/R422A/R430A hAIF_{Δ1–102} aggregation states upon reduction by NADH (Figure SI-2), cartoon representation of the putative NAD(H)_B-binding site on the mAIF_{rd}:NAD(H) complex (Figure SI-3), alternative hypothetical pathway of electrons (Figure SI-4), surface electrostatic potential of hAIF_{Δ1–121ox} and hAIF_{Δ1–102rd}:2NAD(H) (Figure SI-5), surfaces for the interaction of hAIF with other proteins (Figure SI-6) and X-ray data collection and refinement statistics (Table SI-1) in Supporting Results; and Supporting References. This material is available free of charge via the Internet at <http://pubs.acs.org>.

AUTHOR INFORMATION

Corresponding Author

*Phone: +34976762476. Fax: +34976762123. E-mail: mmedina@unizar.es.

Author Contributions

[†]These authors (P.F. and R.V.) contributed equally to this work.

Notes

The authors declare no competing financial interest.

ACKNOWLEDGMENTS

The authors thank I. Echániz and N. Movilla for technical assistance. Spanish MINECO (BIO2010-14983 and BFU2011-25326), Aragonian Government DGA-FSE (B18), Fondation de France, French National Cancer Institute (INCa-5839), French National Research Agency (ANR-12-EMMA-0045), Instituto de Salud Carlos III-FIS (PI 09/00946), Fundación Ramón Areces and ARAID. C.M., R.V., and L.C. thank DGA, MINECO, and ENS-Cachan respectively, for Ph.D. fellowships.

ABBREVIATIONS:

AIF, mAIF, hAIF, hAIF_{Δ1–54} and hAIF_{Δ1–102}, apoptosis inducing factor, murine and human isoforms, and human isoforms after deletion of either the first N-terminal 54 or 102 residues; FAD and FADH₂, oxidized and two-electron reduced forms of flavin adenine dinucleotide; DCPIP, 2,6-dichlorophenolindophenol; WT, wild-type; CTC, charge transfer complex; AFM, atomic force microscopy; SPR, surface plasmon resonance; HT, hydride transfer; MLS, mitochondrial localization sequence; NLS, nuclear leading sequence; BS³, homobifunctional-bis[sulfosuccinimidyl]-suberate; PCD, programmed cell death; Cyt c, cytochrome c; MEFs, mouse embryonic fibroblasts

REFERENCES

- (1) Susin, S. A., Lorenzo, H. K., Zamzami, N., Marzo, I., Snow, B. E., Brothers, G. M., Mangion, J., Jacotot, E., Costantini, P., Loeffler, M., Larochette, N., Goodlett, D. R., Aebersold, R., Siderovski, D. P., Penninger, J. M., and Kroemer, G. (1999) Molecular characterization of mitochondrial apoptosis-inducing factor. *Nature* 397, 441–446.
- (2) Natarajan, S. K., and Becker, D. F. (2012) Role of apoptosis-inducing factor, proline dehydrogenase, and NADPH oxidase in apoptosis and oxidative stress. *Cell Health Cytoskelet.*, 11–27.
- (3) Daugas, E., Nochy, D., Ravagnan, L., Loeffler, M., Susin, S. A., Zamzami, N., and Kroemer, G. (2000) Apoptosis-inducing factor (AIF): a ubiquitous mitochondrial oxidoreductase involved in apoptosis. *FEBS Lett.* 476, 118–123.
- (4) Mate, M. J., Ortiz-Lombardia, M., Boitel, B., Haouz, A., Tello, D., Susin, S. A., Penninger, J., Kroemer, G., and Alzari, P. M. (2002) The

- crystal structure of the mouse apoptosis-inducing factor AIF. *Nat. Struct. Biol.* 9, 442–446.
- (5) Miramar, M. D., Costantini, P., Ravagnan, L., Saraiva, L. M., Haozui, D., Brothers, G., Penninger, J. M., Peleato, M. L., Kroemer, G., and Susin, S. A. (2001) NADH oxidase activity of mitochondrial apoptosis-inducing factor. *J. Biol. Chem.* 276, 16391–16398.
- (6) Lorenzo, H. K., Susin, S. A., Penninger, J., and Kroemer, G. (1999) Apoptosis inducing factor (AIF): a phylogenetically old, caspase-independent effector of cell death. *Cell Death Differ.* 6, 516–524.
- (7) Delettre, C., Yuste, V. J., Moubarak, R. S., Bras, M., Lesbordes-Brion, J. C., Petres, S., Bellalou, J., and Susin, S. A. (2006) AIFsh, a novel apoptosis-inducing factor (AIF) pro-apoptotic isoform with potential pathological relevance in human cancer. *J. Biol. Chem.* 281, 6413–6427.
- (8) Cheung, E. C., Joza, N., Steenaart, N. A., McClellan, K. A., Neuspil, M., McNamara, S., MacLaurin, J. G., Rippstein, P., Park, D. S., Shore, G. C., McBride, H. M., Penninger, J. M., and Slack, R. S. (2006) Dissociating the dual roles of apoptosis-inducing factor in maintaining mitochondrial structure and apoptosis. *EMBO J.* 25, 4061–4073.
- (9) Otera, H., Ohsakaya, S., Nagaura, Z., Ishihara, N., and Mihara, K. (2005) Export of mitochondrial AIF in response to proapoptotic stimuli depends on processing at the intermembrane space. *EMBO J.* 24, 1375–1386.
- (10) Polster, B. M., Basanez, G., Etxebarria, A., Hardwick, J. M., and Nicholls, D. G. (2005) Calpain I induces cleavage and release of apoptosis-inducing factor from isolated mitochondria. *J. Biol. Chem.* 280, 6447–6454.
- (11) Yuste, V. J., Moubarak, R. S., Delettre, C., Bras, M., Sancho, P., Robert, N., d'Alayer, J., and Susin, S. A. (2005) Cysteine protease inhibition prevents mitochondrial apoptosis-inducing factor (AIF) release. *Cell Death Differ.* 12, 1445–1448.
- (12) Delettre, C., Yuste, V. J., Moubarak, R. S., Bras, M., Robert, N., and Susin, S. A. (2006) Identification and characterization of AIFsh2, a mitochondrial apoptosis-inducing factor (AIF) isoform with NADH oxidase activity. *J. Biol. Chem.* 281, 18507–18518.
- (13) Sevrioukova, I. F. (2011) Apoptosis-inducing factor: structure, function, and redox regulation. *Antioxid. Redox Signal.* 14, 2545–2579.
- (14) Ferreira, P., Villanueva, R., Cabon, L., Susin, S. A., and Medina, M. (2013) The oxido-reductase activity of the apoptosis inducing factor: a promising pharmacological tool? *Curr. Pharm. Des* 19, 2628–2636.
- (15) Vahsen, N., Cande, C., Briere, J. J., Benit, P., Joza, N., Laroche, N., Mastroberardino, P. G., Pequignot, M. O., Casares, N., Lazar, V., Feraud, O., Debili, N., Wissing, S., Engelhardt, S., Madeo, F., Piacentini, M., Penninger, J. M., Schagger, H., Rustin, P., and Kroemer, G. (2004) AIF deficiency compromises oxidative phosphorylation. *EMBO J.* 23, 4679–4689.
- (16) Ghezzi, D., Sevrioukova, I., Invernizzi, F., Lamperti, C., Mora, M., D'Adamo, P., Novara, F., Zuffardi, O., Uziel, G., and Zeviani, M. (2010) Severe X-linked mitochondrial encephalomyopathy associated with a mutation in apoptosis-inducing factor. *Am. J. Hum. Genet.* 86, 639–649.
- (17) Berger, I., Ben-Neriah, Z., Dor-Wolman, T., Shaag, A., Saada, A., Zenvirt, S., Raas-Rothschild, A., Nadjari, M., Kaestner, K. H., and Elpeleg, O. (2011) Early prenatal ventriculomegaly due to an AIFM1 mutation identified by linkage analysis and whole exome sequencing. *Mol. Genet. Metab.* 104, 517–520.
- (18) Rinaldi, C., Grunseich, C., Sevrioukova, I. F., Schindler, A., Horkayne-Szakaly, I., Lamperti, C., Landoure, G., Kennerson, M. L., Burnett, B. G., Bonnemann, C., Biesecker, L. G., Ghezzi, D., Zeviani, M., and Fischbeck, K. H. (2012) Cowchock syndrome is associated with a mutation in apoptosis-inducing factor. *Am. J. Hum. Genet.* 91, 1095–1102.
- (19) Lewis, E. M., Wilkinson, A. S., Jackson, J. S., Mehra, R., Varambally, S., Chinnaiyan, A. M., and Wilkinson, J. C. (2012) The enzymatic activity of apoptosis-inducing factor supports energy metabolism benefiting the growth and invasiveness of advanced prostate cancer cells. *J. Biol. Chem.* 287, 43862–43875.
- (20) Churbanova, I. Y., and Sevrioukova, I. F. (2008) Redox-dependent changes in molecular properties of mitochondrial apoptosis-inducing factor. *J. Biol. Chem.* 283, 5622–5631.
- (21) Ye, H., Cande, C., Stephanou, N. C., Jiang, S., Gurbuxani, S., Laroche, N., Daugas, E., Garrido, C., Kroemer, G., and Wu, H. (2002) DNA binding is required for the apoptogenic action of apoptosis inducing factor. *Nat. Struct. Biol.* 9, 680–684.
- (22) Sevrioukova, I. F. (2009) Redox-linked conformational dynamics in apoptosis-inducing factor. *J. Mol. Biol.* 390, 924–938.
- (23) Lorenzo, H. K., and Susin, S. A. (2007) Therapeutic potential of AIF-mediated caspase-independent programmed cell death. *Drug Resist. Updat.* 10, 235–255.
- (24) Sotres, J., Lostao, A., Gomez-Moreno, C., and Baro, A. M. (2007) Jumping mode AFM imaging of biomolecules in the repulsive electrical double layer. *Ultramicroscopy* 107, 1207–1212.
- (25) Fernandez-Vizarra, E., Lopez-Perez, M. J., and Enriquez, J. A. (2002) Isolation of biogenetically competent mitochondria from mammalian tissues and cultured cells. *Methods* 26, 292–297.
- (26) Schagger, H. (1995) Native electrophoresis for isolation of mitochondrial oxidative phosphorylation protein complexes. *Methods Enzymol.* 260, 190–202.
- (27) Acin-Perez, R., Fernandez-Silva, P., Peleato, M. L., Perez-Martos, A., and Enriquez, J. A. (2008) Respiratory active mitochondrial supercomplexes. *Mol. Cell* 32, 529–539.
- (28) Wittig, I., Karas, M., and Schagger, H. (2007) High resolution clear native electrophoresis for in-gel functional assays and fluorescence studies of membrane protein complexes. *Mol. Cell Proteomics* 6, 1215–1225.
- (29) Vonrhein, C., Flensburg, C., Keller, P., Sharff, A., Smart, O., Paciorek, W., Womack, T., and Bricogne, G. (2011) Data processing and analysis with the autoPROC toolbox. *Acta Crystallogr. D Biol. Crystallogr.* 67, 293–302.
- (30) CCP4 (1994) The CCP4 suite: programs for protein crystallography. *Acta Crystallogr. D Biol. Crystallogr.* 50, 760–763.
- (31) Jomain, J. B., Tallet, E., Broutin, I., Hoos, S., van Agthoven, J., Ducruix, A., Kelly, P. A., Kraglund, B. B., England, P., and Goffin, V. (2007) Structural and thermodynamic bases for the design of pure prolactin receptor antagonists: X-ray structure of Del1–9-G129R-hPRL. *J. Biol. Chem.* 282, 33118–33131.
- (32) Macheroux, P. (1999) UV-visible spectroscopy as a tool to study flavoproteins, in *Flavoproteins Protocols* (Stephen, K., Chapman, G. A. R., Ed.), pp 1–7, Humana Press, Totowa, NJ.
- (33) Ferreira, P., Hernandez-Ortega, A., Herguedas, B., Martinez, A. T., and Medina, M. (2009) Aryl-alcohol oxidase involved in lignin degradation: a mechanistic study based on steady and pre-steady state kinetics and primary and solvent isotope effects with two alcohol substrates. *J. Biol. Chem.* 284, 24840–24847.
- (34) Marcuello, C., Arilla-Luna, S., Medina, M., and Lostao, A. (2013) Detection of a quaternary organization into dimer of trimers of *Corynebacterium ammoniagenes* FAD synthetase at the single-molecule level and at the in cell level. *Biochim. Biophys. Acta* 1834, 665–676.
- (35) Modjtahedi, N., Giordanetto, F., and Kroemer, G. (2010) A human mitochondrialopathy caused by AIF mutation. *Cell Death Differ.* 17, 1525–1528.
- (36) Neves, M. A., Yeager, M., and Abagyan, R. (2012) Unusual arginine formations in protein function and assembly: rings, strings, and stacks. *J. Phys. Chem. B* 116, 7006–7013.
- (37) Cande, C., Vahsen, N., Kouranti, I., Schmitt, E., Daugas, E., Spahr, C., Luban, J., Kroemer, R. T., Giordanetto, F., Garrido, C., Penninger, J. M., and Kroemer, G. (2004) AIF and cyclophilin A cooperate in apoptosis-associated chromatinolysis. *Oncogene* 23, 1514–1521.
- (38) Artus, C., Boujrad, H., Bouharrou, A., Brunelle, M. N., Hoos, S., Yuste, V. J., Lenormand, P., Rousselle, J. C., Namane, A., England, P., Lorenzo, H. K., and Susin, S. A. (2010) AIF promotes chromatinolysis and caspase-independent programmed necrosis by interacting with histone H2AX. *EMBO J.* 29, 1585–1599.

- (39) Zhu, C., Wang, X., Deinum, J., Huang, Z., Gao, J., Modjtahedi, N., Neagu, M. R., Nilsson, M., Eriksson, P. S., Hagberg, H., Luban, J., Kroemer, G., and Blomgren, K. (2007) Cyclophilin A participates in the nuclear translocation of apoptosis-inducing factor in neurons after cerebral hypoxia-ischemia. *J. Exp Med.* 204, 1741–1748.
- (40) Gurbuxani, S., Schmitt, E., Cande, C., Parcellier, A., Hammann, A., Daugas, E., Kouranti, I., Spahr, C., Pance, A., Kroemer, G., and Garrido, C. (2003) Heat shock protein 70 binding inhibits the nuclear import of apoptosis-inducing factor. *Oncogene* 22, 6669–6678.
- (41) Matsumori, Y., Hong, S. M., Aoyama, K., Fan, Y., Kayama, T., Sheldon, R. A., Vexler, Z. S., Ferriero, D. M., Weinstein, P. R., and Liu, J. (2005) Hsp70 overexpression sequesters AIF and reduces neonatal hypoxic/ischemic brain injury. *J. Cereb. Blood Flow Metab.* 25, 899–910.
- (42) Collingwood, T. S., Smirnova, E. V., Bogush, M., Carpinio, N., Annan, R. S., and Tsygankov, A. Y. (2007) T-cell ubiquitin ligand affects cell death through a functional interaction with apoptosis-inducing factor, a key factor of caspase-independent apoptosis. *J. Biol. Chem.* 282, 30920–30928.
- (43) Wang, Y., Kim, N. S., Haince, J. F., Kang, H. C., David, K. K., Andraibi, S. A., Poirier, G. G., Dawson, V. L., and Dawson, T. M. (2011) Poly(ADP-ribose) (PAR) binding to apoptosis-inducing factor is critical for PAR polymerase-1-dependent cell death (parthanatos). *Sci. Signal.* 4, ra20.
- (44) Di Lisa, F., Menabo, R., Canton, M., Barile, M., and Bernardi, P. (2001) Opening of the mitochondrial permeability transition pore causes depletion of mitochondrial and cytosolic NAD⁺ and is a causative event in the death of myocytes in postischemic reperfusion of the heart. *J. Biol. Chem.* 276, 2571–2575.
- (45) Rustin, P., Parfait, B., Chretien, D., Bourgeron, T., Djouadi, F., Bastin, J., Rotig, A., and Munich, A. (1996) Fluxes of nicotinamide adenine dinucleotides through mitochondrial membranes in human cultured cells. *J. Biol. Chem.* 271, 14785–14790.

SUPPORTING INFORMATION

Structural insights into the coenzyme mediated monomer-dimer transition of the pro-apoptotic Apoptosis Inducing Factor

Patricia Ferreira^{a,b,1}, Raquel Villanueva^{a,b1}, Marta Martínez-Júlvez^{a,b}, Beatriz Herguedas^{a,b}, Carlos Marcuello^c, Patricio Fernandez-Silva^a, Lauriane Cabon^{d,e,f}, Juan A. Hermoso^g, Anabel Lostao^{c,h}, Santos A. Susin^{d,e,f} and Milagros Medina^{a,b,*}.

^aDepartamento de Bioquímica y Biología Molecular y Celular, Universidad de Zaragoza, Zaragoza, Spain.

^bInstituto de Biocomputación y Física de Sistemas complejos (BIFI)-Joint Unit BIFI-IQFR (CSIC). Universidad de Zaragoza, Zaragoza, Spain.

^cLaboratorio de Microscopias Avanzadas, Instituto de Nanociencia de Aragón (INA). Universidad de Zaragoza, Zaragoza, Spain.

^dINSERM U1138, Cell Death and Drug Resistance in Lymphoproliferative Disorders Team, Centre de Recherche des Cordeliers, F-75006, Paris, France.

^eUniversité Pierre et Marie Curie-Sorbonne Universités, F-75006, Paris, France.

^fUniversité Paris Descartes-Sorbonne Paris

Cité, F-75006, Paris, France.

^gInstituto de Química Física Rocasolano, CSIC, Madrid, Spain.

^hFundación ARAID, Spain.

¹These authors contributed equally to this work

*Correspondence to: Dr. Milagros Medina. Departamento de Bioquímica y Biología Molecular

y Celular. Facultad de Ciencias. Universidad de Zaragoza. 50009-Zaragoza. Spain.

Phone:+34976762476, Fax:+34976762123, e-mail: mmedina@unizar.es

This **Supporting** Information includes methodology about production and purification of hAIF variants, atomic force microscopy imaging, steady-state and transient kinetics analysis, HeLa and MEFs cell cultures, Western blotting and refinement of the hAIF_{Δ1-121ox} structure in

Supporting information of experimental procedures; Evolution of the WT spectrum along photoreduction, and spectra for oxidized WT and E413A/R422A/R430A hAIF_{Δ1-102} (**Figure SI-1**), SDS patterns of WT and E413A/R422A/R430A hAIF_{Δ1-102} aggregation states upon reduction by NADH (**Figure SI-2**), cartoon representation of the putative NAD(H)_B-binding site on the mAIF_{rd}:NAD⁺ complex (**Figure SI-3**), alternative hypothetical pathway of electrons (**Figure SI-4**), surface electrostatic potential of hAIF_{Δ1-102} and hAIF_{Δ1-102rd}:2NAD(H) (**Figure SI-5**), surfaces for the interaction of hAIF with other proteins (**Figure SI-6**) and X-ray data collection and refinement statistics (Table SI-1) in **Supporting Results**; and **Supporting References**.

EXPERIMENTAL PROCEDURES

Production and purification of WT and E413A/R422A/R430A hAIF_{Δ1-102} - 10 L cultures of *E. coli* containing the plasmid with corresponding hAIF_{Δ1-102} gene were grown at 37°C in LB medium containing 30 mg/L kanamycin and 0.08 g/L riboflavin for large-scale purification. At A_{600nm} ≈ 0.8 cultures were induced with 1 mM IPTG (BioChemica), incubated under the same conditions and harvested after 24 h. Cells were resuspended in 50 mM phosphate, pH 8.0 buffer also containing 1 mM phenylmethysulfonyl fluorine, 0.001 mM pepstatin A and 20 mM β-mercaptoethanol, and subsequently sonicated at 4°C. After centrifugation to remove debris, the lysate was mixed with 5 mL of Ni²⁺ IMAC Sepharose affinity resin (GE Healthcare), previously equilibrated in 50 mM phosphate, pH 8.0, buffer containing 10 mM imidazole and 400 mM KCl. This mixture was incubated on a bidirectional orbital rocker for 1 h at 4°C, then loaded into a column, and washed with 50 mM phosphate, pH 8.0, containing 40 mM imidazole and 400 mM KCl. The protein was eluted with a 0.15 L linear gradient from 40 mM to 500 mM imidazole in 50 mM phosphate at pH 8.0. Fractions with A₂₈₀/A₄₅₀ ratios <10-12 were combined, concentrated, and dialyzed with 50 mM phosphate at pH 8.0 to remove imidazole

traces.

Atomic force microscopy imaging- For immobilization samples of WT or E413A/R422A/R430A hAIF_{Δ1-102} were incubated on fresh exfoliated muscovite mica pieces (*Electron Microscopy Sciences*) for 10 min at room temperature. The functionalized mica was then washed with PBS, and the immobilized sample and the cantilever holder were introduced into a liquid cell. Image processing was performed with WSxM (1). Estimation of percentages for the different oligomeric states was calculated as previously described (2). At least 10 images of 10 different areas of 500 nm² were analyzed. Percentages of each species were determined as the existing number of this species with respect to the total number in the sample. The error was calculated from the dispersion of results in the analysis of different images corresponding to different areas of the sample.

Refinement of the hAIF_{Δ1-102rd}:2NAD(H) structure- Refinement was performed automatically with REFMAC by applying non-crystallographic symmetry restraints, and the manual model building was performed using Coot (3, 4). Water molecules were automatically picked and visually checked with Coot. The structure contains 4 AIF monomers in the asymmetric unit, with Matthew's coefficient and solvent content of 3.47 Å³/Da and 64.63 %, respectively.

Refinement of the hAIF_{Δ1-121ox} structure- Inspection of the pdb and mtz files of the previously reported PDB 1M6I corresponding to hAIF_{Δ1-121ox} (5) showed some extra electronic density not assigned to the protein sequence. We used that density to model additional residues to those reported in PDB 1M6I and to improve the orientation of a few side-chains. Refinement was carried out using as initial input files the pdb and mtz files deposited on the PDB for 1M6I with REFMAC and COOT. The final model, deposited with PDB ID: 4BV6, contains residues 127–545 (nine additional residues regarding PDB 1M6I) and 560–608, with one disordered internal stretches and disordered N- and C-terminal tails. Initial and refined structures resemble very much (r.m.s.d. for 459 Cα and 3536 atoms, 0.10 Å and 0.56 Å, respectively). Improvement of side-chains has been particularly relevant for Trp483, buried in the structure at the *si*-face of FAD. In the refined structure Trp483 shows the same conformation as that recently described in

the structure of the E493V mutant (6).

Steady-state kinetics- The steady-state assays were performed in air-saturated 50 mM Tris-HCl, pH 8.0, at 25°C. The NADH oxidase activity was monitored by following NADH consumption at 340 nm ($\epsilon_{340\text{nm}}=6.22 \text{ mM}^{-1}\text{cm}^{-1}$) (7). The NAD(P)H oxidoreductase activity using electron acceptors other than molecular oxygen was tested by the diaphorase activity with 95 μM 2,6-dichlorophenolindophenol (DCPIP) or with 1.25 mM potassium ferricyanide, and the cytochrome *c* (Cyt*c*) reductase activity was tested with 0.375 mg/mL Cyt*c*. Processes were followed at the wavelengths of maximal molar absorption coefficient change for each electron acceptor upon reduction ($\epsilon_{620\text{nm}}=21 \text{ mM}^{-1}\text{cm}^{-1}$, $\epsilon_{405\text{nm}}=1.04 \text{ mM}^{-1}\text{cm}^{-1}$, $\epsilon_{550\text{nm}}=20 \text{ mM}^{-1}\text{cm}^{-1}$, respectively). The ferric, glutathione and quinone reductase activities were monitored by following NADH oxidation at 340 nm and using Fe^{3+} -EDTA (0.5–5 mM), oxidized glutathione (5 mM) and several quinones (200 μM 1,4-benzoquinone, 200 μM 1,2-naptoquinone and 200 μM Coenzyme Q1 and Q10) respectively, as electron acceptors. Steady-state kinetics parameters were determined by fitting initial reaction rates at different NAD(P)H concentrations to the Michaelis-Menten equation for one substrate, $v = k_{\text{cat}} \cdot S / (K_m + S)$, where K_m represents the Michaelis constant, and k_{cat} the maximal turnover number of the enzyme. Errors in the determination of steady state constants were within $\pm 10\%-20\%$.

Transient kinetics analysis- Spectral evolution analysis was performed by global analysis and numerical integration methods fitting the collected data to a single step, A→B, model, allowing estimation of the observed reduction rate constants (k_{obs}). When a saturation profile on the coenzyme concentration was observed, k_{obs} values were fitted to the $k_{\text{obs}} = k_{\text{HT}} \cdot S / (K_d + S)$ equation describing formation of an enzyme:substrate complex previous to the electron transfer process, where k_{HT} is the limiting rate constant for the hydride transfer (HT) from the pyridine nucleotide coenzyme to the FAD cofactor of hAIF, and K_d is the hAIF:coenzyme dissociation constant. Errors in the determination of K_d were below $\pm 15\%-20\%$, while those of k_{obs} and k_{HT} values were below $\pm 10\%$.

Cell cultures for determination of the *in vivo* association state of AIF- HeLa and MEF cells were grown in Dulbecco's modified Eagle's medium (DMEM, Gibco) and in

DMEM+GlutaMAX medium, respectively, with 50 units/mL penicillin, 50 mg/mL streptomycin and supplemented with fetal bovine serum (FBS) at a final concentration of 10%. Cell cultures were performed in a 5% CO₂ atmosphere at 37 °C.

Western blot - For Western blot analysis of cell extracts, equal amounts of total proteins, with concentrations determined using the BioRad Protein Assay, were loaded either on high-resolution clear native electrophoresis-1 gels or on linear SDS-PAGE gels, respectively, and transferred onto Hybond-P PVDF membranes (GE Lifesciences). Membrane blocking and antibody incubations were performed in PBS 0.1% Tween 20 plus 5% non-fat dry milk. Antibody used was anti-AIF (Invitrogen). Immunoreactive proteins were detected using HRP-conjugated secondary antibodies, peroxidase-conjugated anti-mouse or anti-rabbit (Invitrogen). Signal was detected using the EZ-ECL Chemiluminiscence Detection kit from HRP (Biological Industries), and immunoblot images were obtained in a Bio-Imaging System MF-ChemiBis 4.2.

Data analysis- Data were fitted with SigmaPlot (Systat Software Inc. Richmond, CA, USA), and Pro-K (Applied Photophysics Ltd.)

SUPPORTING RESULTS

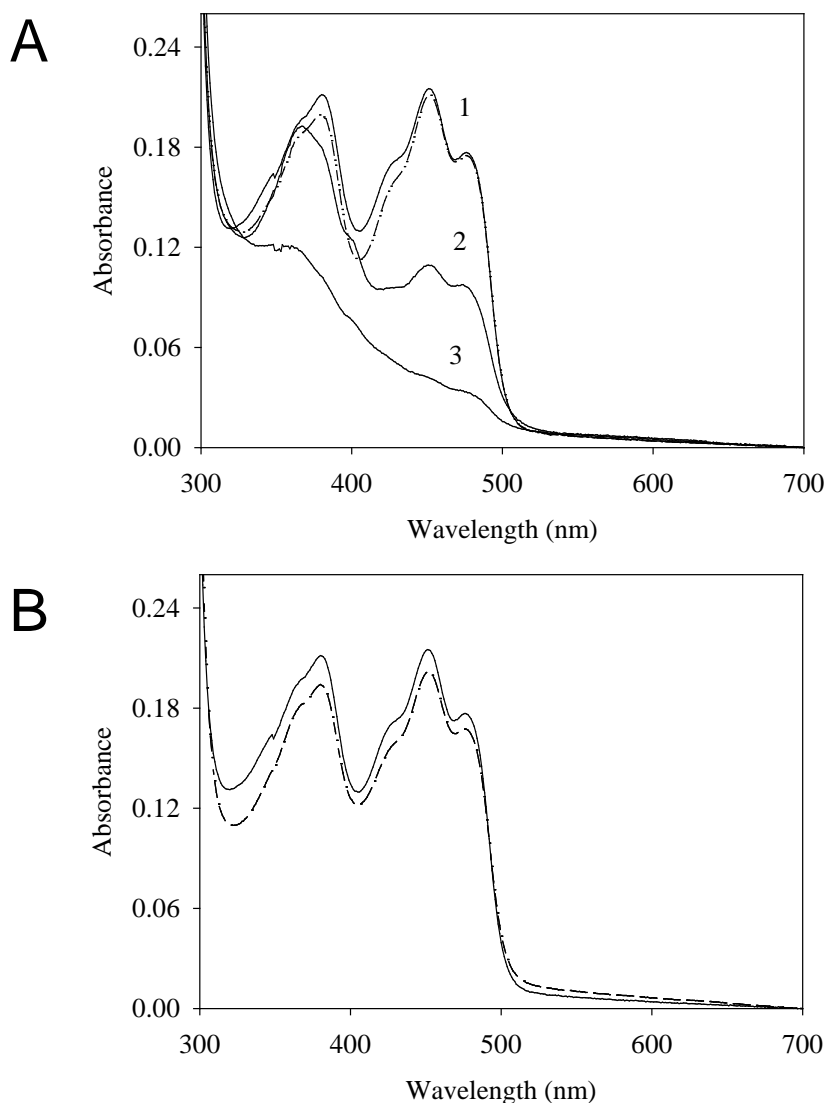


Figure SI-1. A. Evolution of the visible spectrum of hAIF_{Δ1-102} along photoreduction. Trace 1 shows the anaerobic spectrum of 15 μ M hAIF_{Δ1-102ox} before illumination, while traces 2 and 3 show the spectra after 24 min and 118 min of illumination, respectively. The spectrum of reoxidized hAIF_{Δ1-102} recorded after opening the cuvette to the air is shown by a dashed line. B. Absorption spectra of hAIF_{Δ1-102} WT (dotted line) and E413A/R422A/R430A hAIF_{Δ1-102} (dashed line). All the spectra were obtained in 50 mM Tris-HCl, pH 8.0.

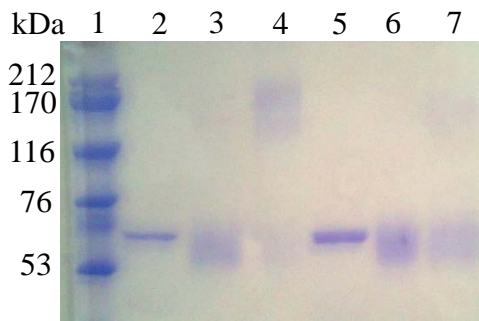


Figure SI-2. SDS patterns of WT and E413A/R422A/R430A hAIF $_{\Delta 1-102}$ aggregation upon reduction by NADH. Line 1: protein markers; line 2: WT protein, line 3: WT treated with BS³, line 4: WT treated with NADH and BS³, line 5: E413A/R422A/R430A variant, line 6: E413A/R422A/R430A variant treated with BS³, line 7: E413A/R422A/R430A variant treated with NADH and BS³.

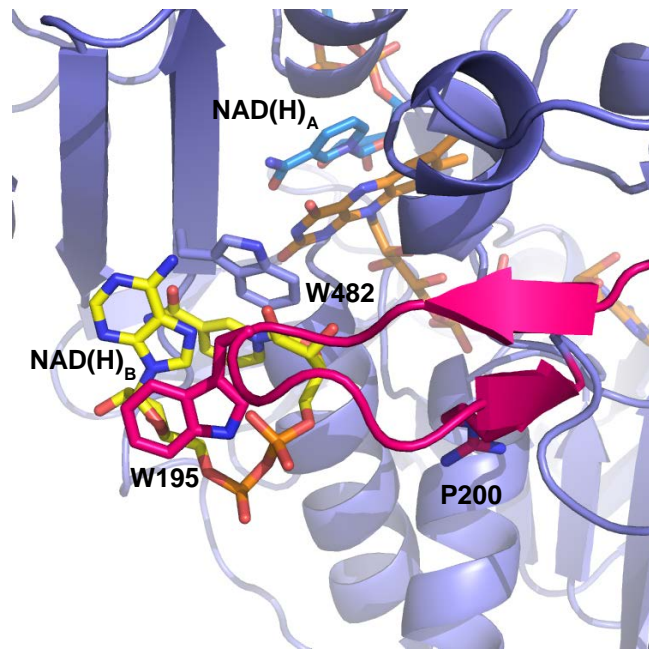


Figure SI-3. Cartoon representation of a detail of the putative binding of NAD(H)_B on the crystal mAlF_{rd}:NAD⁺ complex (PDB, 3GD4, shown with violet ribbons) in the best pose predicted with the Swiss-Dock server (8). R200, W194 and W482 (corresponding to R201, W196 and W483 in the human enzyme) are shown as sticks and CPK colored. FAD, NAD(H)_A and NAD(H)_B are drawn in sticks with C in orange, blue and yellow, respectively. The β -hairpin is in hot pink.

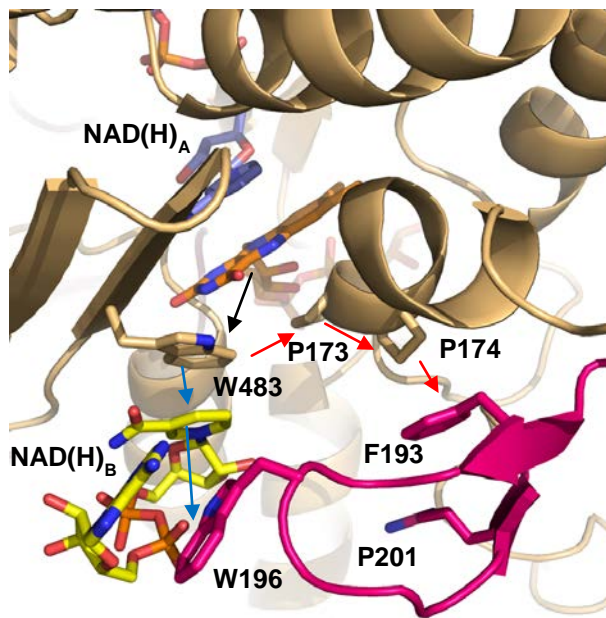


Figure SI-4. Alternative hypothetical pathway for the electrons coming from the flavin ring to the surface via W483. Residues of the β -hairpin are in hot pink. FAD, NAD(H)_A and NAD(H)_B are drawn in sticks with C in orange, blue and yellow, respectively. Residues involved in the putative pathways are shown in CPK sticks. Black arrows shows the initial transfer to W483, beyond this point red arrows show the pathway proposed with the mAlF_{rd}:NAD(H) structure (9), while blue arrows indicate an alternative one via the nicotinamide of NAD(H)_B.

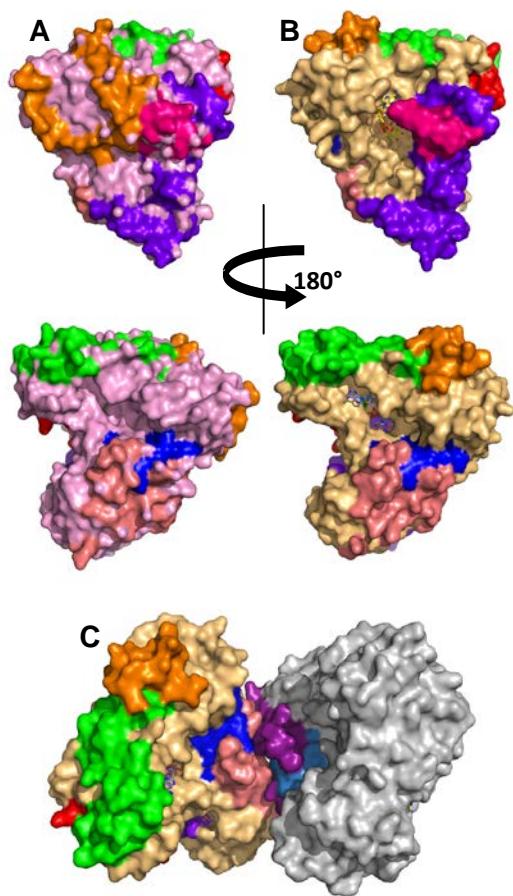


Figure SI-5. Modifications induced by dimerization at the surfaces of interaction of hAIF. Surface representation of the structures of (A) hAIF_{Δ1-121_{ox}} (pink) and (B) hAIF_{Δ1-102_{rd}}:2NAD(H) (wheat). The 508-560 surface is in orange, the dimerization surface is in dark salmon, the β-hairpin surface is in hot pink, the proposed interaction surface with CypA (residues 345-397) is in green, the proposed interaction surface with Hsp70 (residues 150-228 with exception of the β-hairpin) is in violet, NLS1 surface is in red and NLS2 surface is in blue. FAD, NAD(H)_A and NAD(H)_B are drawn in sticks with C in orange, blue and yellow, respectively. (C) Surface representation of the hAIF_{Δ1-102_{rd}}:2NAD(H) dimer. Protomer corresponding to chain A is colored as about mentioned, while that corresponding to chain C is colored in grey with the dimerization surface and the NLS2 in magenta and metallic blue, respectively.

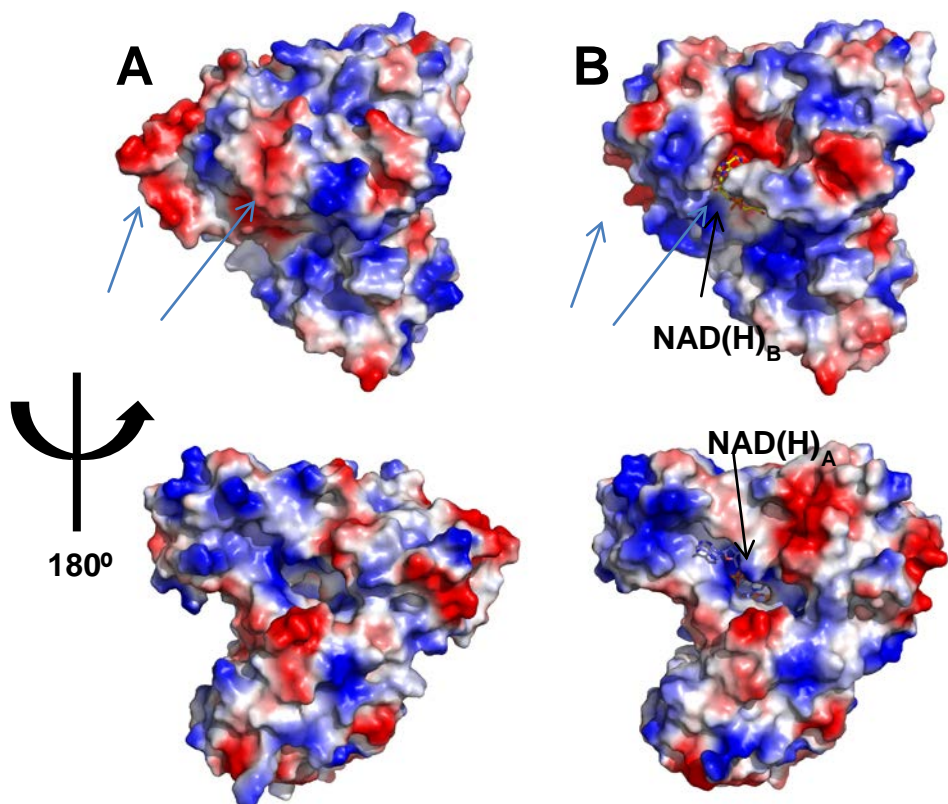


Figure SI-6. Surface electrostatic potential of (A) hAIF_{Δ1-102} and (B) hAIF_{Δ1-102rd:2NAD(H)}. In (B) NAD(H)_A and NAD(H)_B are drawn in sticks with C in blue and yellow, respectively and indicated with a black arrow. Positions where major changes are observed are indicated with blue arrows.

Table SI-1. X-ray data collection and refinement statistics

Crystal data	hAIF _{Δ1-102rd} :2NAD(H)	hAIF _{Δ1-121ox} ^c	
Space group	P3 ₂ 21	P2 ₁	
Unit Cell Parameters (Å)	a=b=120.7, c= 343.4	a= 50.9, b= 90.5, c= 60.5	
Data Collection			
Temperature (K)	100	110	
Beamline	ID23-1 ESRF	APS 19-ID	
Wavelength (Å)	0.97626	0.9793	
Resolution (Å)	343.36-2.88 (3.04-2.88)	40-1.9	
Total reflections	442087	44,620	
Unique reflections	66505	-	
Mean I/σ(I)	12.6 (3.4)	-	
Completeness (%)	99.8 (100)	99.1 (98.0)	
Redundancy	6.6 (7.0)	-	
R _{sym} ^a	0.105 (0.467)	0.059 (0.258)	
Data Refinement			
Resolution range (Å)	40-2.88	40-1.8	
Number of atoms			
Protein	13769	3526	3649
Ligand	569	53	59
Solvent	24	235	289
R _{work} (%)	17.6	22.5	19.4
R _{free} ^b (%)	23.0	24.2	21.5
r.m.s.d. bond lenght (Å)	0.009	0.006	0.009
r.m.s.d. bond angles (°)	1.479	1.3	1.3
Average B-factor (Å ²)	56.7	-	17.4
Ramachandran analysis			
In allowed regions (%)	98.6	99.3	99.4
Outlet %	1.4	0.7	0.6

Values in parentheses correspond to the highest resolution shell.

^a R_{sym} = Σ|I - I_{av}| / Σ I, where the summation is over symmetry equivalent reflections.

^b R calculated for 7% of data excluded from the refinement.

^c Data collection from 1M6I. For data refinement first column shows data taken from 1M6i pdb, while second column has been produced in the present work.

References

1. Horcas, I., Fernandez, R., Gomez-Rodriguez, J. M., Colchero, J., Gomez-Herrero, J., and Baro, A. M. (2007) WSXM: a software for scanning probe microscopy and a tool for nanotechnology, *Rev Sci Instrum* 78, 013705.
2. Marcuello, C., Arilla-Luna, S., Medina, M., and Lostao, A. (2013) Detection of a quaternary organization into dimer of trimers of *Corynebacterium ammoniagenes* FAD synthetase at the single-molecule level and at the in cell level, *Biochim Biophys Acta* 1834, 665-676.
3. Emsley, P., and Cowtan, K. (2004) Coot: model-building tools for molecular graphics, *Acta Crystallogr D Biol Crystallogr* 60, 2126-2132.
4. CCP4. (1994) The CCP4 suite: programs for protein crystallography, in *Acta Crystallogr D Biol Crystallogr* 1994/09/01 ed., pp 760-763.
5. Ye, H., Cande, C., Stephanou, N. C., Jiang, S., Gurbuxani, S., Laroquette, N., Daugas, E., Garrido, C., Kroemer, G., and Wu, H. (2002) DNA binding is required for the apoptogenic action of apoptosis inducing factor, *Nat Struct Biol* 9, 680-684.
6. Rinaldi, C., Grunseich, C., Sevrioukova, I. F., Schindler, A., Horkayne-Szakaly, I., Lamperti, C., Landoure, G., Kennerson, M. L., Burnett, B. G., Bonnemann, C., Biesecker, L. G., Ghezzi, D., Zeviani, M., and Fischbeck, K. H. (2012) Cowchock syndrome is associated with a mutation in apoptosis-inducing factor, *Am J Hum Genet* 91, 1095-1102.
7. Miramar, M. D., Costantini, P., Ravagnan, L., Saraiva, L. M., Haouzi, D., Brothers, G., Penninger, J. M., Peleato, M. L., Kroemer, G., and Susin, S. A. (2001) NADH oxidase activity of mitochondrial apoptosis-inducing factor, *J Biol Chem* 276, 16391-16398.
8. Grosdidier, A., Zoete, V., and Michelin, O. (2011) SwissDock, a protein-small molecule docking web service based on EADock DSS, *Nucleic Acids Res* 39, W270-277.
9. Sevrioukova, I. F. (2009) Redox-linked conformational dynamics in apoptosis-inducing factor, *J Mol Biol* 390, 924-938.